Title.

A hippocampal astrocytic sequence emerges during learning and memory

Authors. Ryan A. Senne*[1,2,3], Rebecca L. Suthard* [1,3], Rui Cao[3,] Amy H. Monasterio[1,3], Evan A. Reusch[4], Michelle D. Buzharsky[1,3], Marc W. Howard[3], Steve Ramirez [2,3]

Affiliations.

[1]Graduate Program for Neuroscience, Boston University, Boston, MA 02215
[2]Department of Biomedical Engineering, Boston University, Boston, MA 02215
[3]Department of Psychological and Brain Sciences, The Center for Systems Neuroscience, Neurophotonics Center, and Photonics Center, Boston University, Boston, MA 02215
[4]Department of Brain and Cognitive Sciences, Massachusetts Institute of Technology, Cambridge, MA 02139
These authors contributed equally to this work

Corresponding author. Steve Ramirez, PhD; dvsteve@bu.edu

Abstract.

The dorsal hippocampus is a heterogeneous structure with numerous cell types involved in generating and maintaining detailed representations of space and time. Prior work has established that pyramidal cells contribute to these crucial aspects of episodic memory. For example, hippocampal “time cells” encode temporal information through sequential activity. However, the role of non-neuronal cell types are less often explored. In this study, we investigated dorsal hippocampal CA1 astrocytes using one-photon calcium imaging in freely moving animals during a contextual fear conditioning paradigm. To our knowledge, this is the first time a study has successfully performed longitudinal registration of astrocytic cell population using 1p calcium imaging, thus permitting the tracking of a stable population of these cells in freely-moving mice. In response to foot shock, astrocytes generated robust calcium-event sequences with a time-compressed structure akin to canonical hippocampal time cells. Upon re-exposure to the conditioned context, these astrocytic sequences persisted in the absence of shock, maintaining their time-compressed structure. Moreover, astrocytes active on the previous day retained a preserved sequential structure, indicating memory-specific properties. This phenomenon was not observed in a context different from the initial fear conditioning chamber. Taken together, these results present a potentially paradigm-shifting notion that astrocytes play a significant role in the representation of temporal information processing across learning and memory.

Introduction.

To create episodic memories with high granularity, the hippocampus must encode information by indexing the spatial and temporal aspects of an experience. Within the hippocampus, pyramidal cells function as place and time cells, developing spatially-tuned receptive fields within an environment or tiling the temporal plane thorough sequential activity[1–6]. Glial cells, on the other hand, have been largely ignored in this realm of spatiotemporal processing until recently. Recent findings have shown that astrocytes interface with neurons in a synergistic and complementary manner to represent spatial information in dorsal CA1 of the hippocampus (dCA1) and may encode reward location via similar spatial mechanisms[7,8]. Further, computational modeling has proposed that astrocytic neuromodulation is sufficient to generate neuronal place fields via enhanced theta oscillations and plasticity changes[9]. Together, these findings open the door to studying astrocytic involvement in spatiotemporal processing during memory formation and retrieval and how it relates to neuronal activity within these circuits.

To investigate the role of astrocytes in spatiotemporal processing within the hippocampus during memory encoding and recall, we employed one-photon (1p) imaging in the dCA1 region. First, we tracked hundreds of astrocytes across days to measure how their activity evolves across learning and memory and

observed that astrocytes are shock-responsive in dCA1 at the single-cell level. Strikingly, we found evidence of astrocyte sequences that are triggered by the onset of aversive foot shocks during contextual fear conditioning (CFC). Moreover, these sequences exhibited similar properties to those displayed by canonical hippocampal time cells in response to other types of stimuli. Finally, these sequences reappeared during contextual recall and showed an inverse relationship with freezing behavior. These findings suggest a role for astrocytes in temporal coding within hippocampal circuits and may serve as a behaviorally relevant memory retrieval mechanism.

Results.

One-photon imaging of dorsal hippocampal astrocytes across contextual fear learning.

To study how astrocytes are involved in temporal coding within a contextual fear conditioning (CFC) paradigm, we performed 1p calcium imaging of dCA1 astrocytes in freely-moving mice (**Figure 1A)**. Wild type, C57BL/6J, male mice were injected with an astrocyte-specific genetically-encoded calcium indicator, AAV5-GfaABC1D-cyto-GCaMP6f, into unilateral dCA1. After recovery and viral expression, a gradient index (GRIN) lens was implanted above the pyramidal cell layer of dCA1 for visualization of the GCaMP-expressing astrocytes (**Figure 1A-B**). Selective expression of GCaMP in astrocytes was assessed with co-staining of neurons (NeuN) or astrocytes (glial fibrillary acidic protein; GFAP). We observed successful labeling of astrocytes in and around the pyramidal cell layer (**Figure 1C**).

On Day 1 of behavior, all mice (n = 7) underwent CFC in Context A (Cxt A) to acquire the association between the conditioned stimulus (context; CS) and unconditioned stimulus (foot shock; US) which were paired at the 120, 180, 240 and 300s time points during a 330s session (foot shocks; 2s duration; 0.75mA intensity) (**Figure 1A**). On Day 2, mice were split into two groups where they were placed back into Cxt A for recall (Cxt A) or into a novel Context B (Cxt B) for the same duration of time each of those days to control for the memory-specific nature of our findings and the effects of time (**Figure 1A**). Behaviorally, there was a significant interaction of Day and Group, as well as a main effect of Group for average freezing levels (**Figure 1D; Supplemental Figure 1A-B)**(Two-way RM ANOVA; [Interaction] $F(1,5) = 21.68$, $p=0.0056$; [Day] $F(1,5) = 2.232$, $p=0.1954$; [Group] $F(1.5) = 10.17$, $p=0.0243$; [Subject] $F(5,5) = 2.269$, $p=0.1948$). Post-hoc multiple comparisons showed that mice in both groups froze at the same level on Day 1 during CFC, as expected (**Figure 1D;** Sidak's multiple comparisons [Day 1]: $p = 0.9960$). While on Day 2, mice in the Cxt A group froze significantly more than the Cxt B group, as they were re-exposed to the fearful context (**Figure 1D;** Sidak's multiple comparisons [Day 2]: $p = 0.0008$).

To assess the role of astrocytes that were reactivated across learning, we longitudinally tracked regions-of-interest (ROIs) from each imaging session. We successfully tracked these astrocytes across days using a combination of manual ROI selection within each session and CellReg, a Matlab-based tool that aligns cell footprints across sessions using field-of-view (FOV) alignment and probabilistic modeling of spatial footprints[10]. CellReg identified astrocytes active on Day 1 or Day 2 only, as well as those that overlapped or were 'reactivated' on Day 2. A representative footprint map shows all cells active during CFC from a FOV that were detected using manual ROI selection (**Figure 1E**). Identification of tracked cells across days of behavior are shown in a representative output image from CellReg, where green ROIs were detected across both sessions (**Figure 1F**).

We next tracked astrocytes across days and observed no significant difference in the total number of active cells on Day 1 vs. Day 2 (Day) or across Cxt A or B (Group) (**Figure 1G**) (Two-way RM ANOVA; [Day x Group] $F(1,5) = 0.8621$, $p=0.3958$; [Day] $F(1,5) = 3.106$, $p=0.1383$; [Group] $F(1,5) = 0.01765$, $p=0.8995$; [Subject] $F(5,5) = 6.410$, $p=0.0312$). Further, tracking of astrocytes across days allowed us to quantify the percentage of cells that were 'reactivated' or present on both days. We hypothesized that there would be more reactivated cells in the Cxt A group because they were placed back into the original fearful context, compared to the Cxt B group. However, we found that there was no significant difference in the percentage of reactivated cells (%reactivated cells/total cells on Day 1) (**Figure 1H;** Independent t-test: $t = 0.1211$, $df=5$, $p=0.9083$).

Together, we show for the first time that tracking of astrocytes across days during 1p imaging is technically possible using our pipeline. Additionally, we conclude that there is a similar number of cells active across CFC and Day 2 in our groups, where a larger sample size may reveal a drop in active cells in the Cxt B group.

Evidence of astrocytic temporal sequences after foot shock onset

To understand the nature of astrocytic single-cell activity during CFC, we first plotted representative individual traces from each group to visualize broad patterns across the session (**Figure 2A**). We observed high-density activity in response to foot shocks, albeit noticing heterogeneous profiles in the individual cell calcium physiology (**Figure 2A**). Qualitatively, single astrocytes displayed unique kinetics and differences in the number of shocks they respond to within a session (**Figure 2A**). When visualizing the average calcium trace for each group, we observed that astrocytes were significantly activated after the onset of each foot shock, peaking around 5 seconds post-stimulus (**Figure 2B;** foot shock peri-event analysis; tCI 95% CI). This finding is in line with previous work from our lab and others showing astrocyte shock response in the hippocampus, cortex, and amygdala[11–13].

Our current experiments allowed us to probe deeper into this population-level shock response, uncovering how subpopulations of astrocytes respond to aversive stimuli. To assess the qualitative variability in astrocytic shock response, we initially performed exploratory dimensionality reduction and clustering using WaveMAP, a method used for unsupervised detection of unique physiological waveform characteristics in electrophysiological and calcium imaging data[14,15] (**Supplemental Figure 2**). Here, we combined all single cell data from all animals (Cxt A and Cxt B) during CFC, as they all underwent the same experimental conditions at this point in testing. Next, we extracted –7.5 to 15 seconds around each foot shock, generated the average shock response for all astrocyte calcium traces, and normalized this data by z-scoring. Thus, we fed our single-astrocyte, average shock response traces across all animals during CFC into the WaveMAP pipeline. After optimizing WaveMap parameters, we found that the data consisted of 8 unique clusters **(Supplemental Figure 2A, C-D**). When we plotted the average shock-response for each cluster, we observed that the peaks of astrocytic calcium waveforms appeared sequential in nature, with the width of the events increasing with time from shock (**Supplemental Figure 2B**). Notably, such features are characteristic of hippocampal time cells[5,6,16–19]. Importantly, these clusters were not driven by individual differences across animals, as noted by distributed representation of all animals within each cluster (**Supplemental Figure 2E**).

Robust astrocytic sequences emerge and tile the interval after foot shock for up to tens of seconds.

Given the physiologically heterogenous astrocytic clusters that WaveMAP revealed, we next investigated the possibility that astrocytic cell populations' calcium events follow a sequential pattern akin to time cells, as opposed to functionally discrete cell populations implied by clustering approaches. First, we plotted the cosine-similarity of each pair of astrocytes in time, sorted based on the time point of their highest activity (**Figure 2C, Supplemental Figure 7A**). The block-like structure emerges after the first foot shock and repeated for subsequent shocks, suggesting a robust neural coding for the shock events with merely one exposure. Furthermore, time immediately after shock is marked by low off-diagonal similarity, suggesting that the neural dynamics change quickly with time, an indication of sequential activity.

To further investigate the stability of a putative astrocytic calcium event sequence in response to foot shock, we first plotted a heatmap using the argmax of each astrocytic calcium trace for Shocks #1 and 3 (Odd) and sorted them based on themselves (**Figure 2D, left; Supplemental Figure 3)**. Next, we plotted this same activity for odd shocks and sorted them based on the argmax of each astrocyte calcium trace for Shocks #2 and 4 (Even) (**Figure 2D, right; Supplemental Figure 3**). To quantitatively assess these results, we calculated the Spearman's correlation coefficients between the true peak times (Odd sorted on Odd) and the cross-validated peak times (Odd sorted on Even) for each animal and found that there was a significant difference between the average rho value and zero (**Figure 2E;** One-sample t-test: $t=13.19$, $p<0.0001$). Next, we fit a linear regression model for all animals to determine if these true peak times and

the cross-validated peak times were related and found a significant relationship between these variables (**Figure 2F; Supplemental Figure 3)**.

To further investigate this potential sequential activity, we fit a hierarchical Bayesian model to the astrocyte calcium activity by assuming an increased activity during a Gaussian-shaped temporal receptive field with the peak location (μ) and receptive field width (σ) for each individual cell after the presentation of foot shock *(see Methods*). Similar models have been applied to hippocampal time cells to investigate the sequential activities of a neural population[19]. To broadly understand the distribution of the model's predicted peaks (μ), we plotted a density histogram of the locations across all animals in Cxt A and Cxt B (n = 7) during CFC (**Figure 2G**). Here, we observed a similarly skewed distribution after the onset of foot shocks that provided evidence of temporal compression. Next, we sorted the average astrocytic response based on their peak location (μ) and observed robust sequences after foot shock in all mice, spanning tens of seconds post-stimulus (peak distribution median = 4.7s with interquartile between 3.5 to 7.2s and 90th percentile = 16.4s) (**Supplemental Figure 4)**. This temporal structure resembled canonical hippocampal time cells, where peak (μ) distribution skews towards smaller values and time field width (σ) increase for cells peak later in the sequence, suggesting a compressed temporal representation (**Supplemental Figure 4**)[5,6].

To test our hypothesis that astrocytes sequences could display time-cell-like properties, we first fit the distribution of estimated μ's to the following probability distributions: Power-law, Exponential, Log-Normal, and Gaussian. When fitting the population peak distribution models, we eliminated cells that peaked during the foot shock duration (<2 s, 1.7% cells eliminated). The fits were evaluated with Watanabe-Akaike Information Criterion (WAIC[20]) and plotted in the cumulative density function (CDF) (**Figure 2H**). Importantly, the Gaussian distribution provided the worst model fit (WAIC=9854), indicating that any sequential activity is not just noisy estimation (**Figure 2H**). Instead, models that have been previously identified in hippocampal time cell sequences such as the Power-law provide a significantly better fit (WAIC=7879), where lower WAIC values indicate 'better' model fit (**Figure 2H**)[19,21]. Note that even the best fitting model, the Power-law, failed to perfectly capture the peak distribution according to a Kolmogorov-Smirnov test (KS distance = 0.46, $p<0.001$), indicating the sequence observed in astrocytes might serve different functions than those of hippocampal time cells. Finally, to quantify the relationship between the peak location and width in our data, we fit a random intercept, linear mixed-effects model, where the receptive field width was a function of the peak location (**Figure 2I**). We note that the width increases linearly with peak (slope=0.364, $p<0.001$), suggesting that the later part of the sequence is represented with lower resolution. Together, these modelling results provide quantitative evidence that these observed sequences are temporally compressed, in-line with findings of hippocampal time cells[6,16,17,19].

Robust sequences spontaneously emerge only when animals return to the conditioned context.

We next set out to understand if these astrocytic sequences were also present during the recall session of behavior, and if so, how they may be memory-specific in nature. To accomplish this, we first plotted representative single-cell activity of astrocytes across both Cxt A and B groups (**Figure 3A**). Here, we qualitatively observe that astrocytes across groups are distinctly different in their calcium responses, with more events occurring in Cxt A, when the mouse is placed back into the conditioned context (**Figure 3A**). We then wanted to test the hypothesis that the temporally compressed sequences noted during CFC would be also present when animals were placed in the same context they were originally fear conditioned in (i.e., Cxt A), but not when placed in a novel context (i.e., Cxt B).

We first plotted the cosine similarity for each animal, as we did previously for CFC, to determine if repeated structures were present in the astrocytic population. After plotting each animal, we found that off diagonal elements were still present and that animals who were exposed to the same context had more structured cosine-similarity plots (**Figure 3B-C; Supplemental Figure 7B).** These findings indicated that sequences were still present in the recall sessions, despite the absence of a discrete, unimodal external stimulus to trigger memory recall.

As no stimulus was present during recall sessions, we developed a method to detect putative spontaneously evoked sequences. Based on our results from CFC and noting that sequences occur when cells are co-active in short succession, we built an "event detector" by summing cell activity over each time index. We then reasoned that sequences would be indicated in this summed activity trace by periods of time wherein the cell activity would be over some threshold of summed activity from the mean (*see Methods*). We then labelled any time index wherein the summed activity trace value at that point was greater than 1.5 standard deviations above the mean of the entire trace. Then, after labelling all indices as meeting this requirement or not, we performed temporal thresholding where indices had to be coincident for 1.0 second to qualify as an "event" (**Figure 3D**). To validate our detector, we first applied this method to the summed-activity traces from CFC and found that our method reliably detected all the shock-triggered sequences that went into our subsequent analysis (**Supplemental Figure 8A**). Next, we performed the same analysis but now on the summed activity traces from the recall session. Here, we detected high-activity events sequences in all animals regardless of context (**Figure 3E-F, Supplemental Figure 8B)**. Importantly, despite the detection of events in both contexts, this did not indicate that both sets of putative sequences hold the same properties (e.g., temporal compression) as our method only detects some increase from baseline activity over a chosen threshold. To quantify the relationship between the shock-triggered sequences in fear conditioning and the spontaneously emerged sequences during recall, we applied the same tests and hierarchical models from CFC to these detected "sequences" across both contexts.

Context-dependent stability of cellular activity across sequences during recall

In CFC, we found that the peak cellular activity of the cells in the sequences induced by foot shocks was correlated across shocks (**Figure 2D-E**). To determine if this result held during recall, we plotted cross-validated heatmaps of the cellular activity in the same way as during CFC i.e., we plotted the heatmap based on the true sorted peak times (Odd sorted on Odd), and plotted it sorted on the even sequence order (Odd sorted on Even) (**Figure 3H-I; Supplemental Figure 5**). We found that the heatmaps of animals re-exposed to Cxt A were far more structured; we again computed the individual Spearman's correlation coefficients of the true peak times and the cross validated peak times, and found that the sequences of animals in Cxt A were significantly more correlated than the animals in Cxt B, as indicated by individual rho values (**Figure 3G;** Independent t-test: t=5.45, p=0.0028). Overall, this indicates that the sequences detected in animals who were re-exposed to Cxt A share a similar stability across events that is akin to what we observed in response to foot-shock the day prior.

Temporal compression of sequences persists in the conditioned context

To further understand the properties of these recall sequences, we fit the same hierarchical Bayesian model used for CFC but separated by Cxt A (n = 4) and Cxt B (n = 3) groups (*see Methods*). To broadly understand the distribution of each model's predicted peaks (μ), we plotted a density histogram of the locations for both Cxt A and B (**Figure 3J)**. Qualitatively, we observe that the distribution of predicted peaks for Cxt A appears more like the distribution present during CFC, suggesting that this activity may also be temporally-compressed **(Figure 3J, 2D**). On the other hand, the distribution for Cxt B appeared more normally distributed (**Figure 3J)**. Next, we sorted the average astrocytic response based on their peak location (μ) and observed robust spontaneous sequences only in the Cxt A mice that appeared like those on the prior day (peak distribution median = 7.7s with interquartile between 5.11 and 11.15s and 90th percentile = 15.3s) (**Supplemental Figure 6**).

We then quantitatively assessed if these sequences in Cxt A similarly carried a compressed timeline as they did during CFC by fitting the same four distributions (e.g. Normal, LogNormal, Exponential and Power-Law) and evaluated the fit with WAIC. Consistent with the results from CFC, the peak distribution in Cxt A was temporally compressed, being best described by a LogNormal distribution (**Figure 3K;** WAIC=4318). A K-S test further supported this fit, showing no evidence of lack-of-fit (KS distance = 0.03, p

= 0.89), reinforcing that the peak distributions were well-represented by the LogNormal model and thus, temporally compressed.

In contrast, animals exploring the novel Cxt B were best described by a Gaussian distribution, suggesting that the detected putative sequences were just white noise and not temporally-compressed (**Figure 3L;** WAIC=3101). The K-S test for Cxt B similarly showed no evidence of lack-of-fit (KS distance=0.07, p=0.12), supporting the Gaussian model's adequacy for these data. In summary, despite the increased noise in the model estimation for recall data, the detected sequences in Cxt A, when animals were re-exposed to the original fear context, are quantitatively different in their peak distributions compared to Cxt B, displaying robust, temporally compressed structure.

Parameter analysis further supports sequence stability across spontaneous events

In our hierarchical Bayesian model, we separately estimated the peak locations for each event, whether driven by a foot shock or occurring spontaneously. This approach allowed us to assess the consistency of temporal information for each cell by estimating an individual standard deviation (SD) parameter for the peak locations across events. A lower SD indicates that a cell's peak activity occurs at a more consistent point within the sequence of events, reflecting greater stability. Based on our non-parametric analyses (**Figure 3H-I**), we hypothesized that cells from animals re-exposed to the familiar context (Cxt A) would show less variability in their peak locations compared to those in the novel context (Cxt B). Our findings confirmed this hypothesis: animals re-exposed to Cxt A had significantly lower variability (median SD) in their peak locations across events than those exposed to Cxt B (**Figure 3M;** Independent t-test: t = 5.87, p=0.025). This indicates that astrocytic sequences are more stable in a familiar, conditioned context compared to a new one, reinforcing the results of our earlier analysis (**Figure 3H-I**).

Neural and behavioral evidence linking CxtA sequences to conditioned memory

Given the structural similarity between the sequences in Cxt A and those observed during CFC, we conducted additional analyses to explore their potential relationship with contextual memory. Our approach consisted of two complementary analyses: first, at the cellular level, to assess whether the structured cellular activity observed during CFC was correlated with the sequence order in the reactivated cell population during recall on the following day. Second, we aimed to determine if these detected sequences in Cxt A were related to the manifestations of fear during contextual recall, specifically by examining freezing behavior.

First, we wanted to understand if the spontaneously detected sequences are related to animal behavior. Prior work from our lab and others has shown that astrocytic activity is often temporally correlated with behavioral epochs[11,12,22–25]. First, we found that mice did not exhibit substantial freezing in Cxt B (**Figure 1D**), where robust sequences are also absent, as reported above. In contrast, we observed both robust sequences and substantial freezing for mice who were re-exposed to Cxt A, suggesting a correlation between these robust sequences and fear memories. First, we plotted epochs of freezing on top of the summed activity traces to note the presence (or lack thereof) of freezing in relation to detected sequence events (**Figure 4A; Supplemental Figure 9)**. Interestingly, in line with our prior observations, it appeared that freezing was less apparent during sequences. To test this hypothesis, we calculated the average percent freezing during a detected spontaneous sequence and outside of this time-period for animals who were re-exposed to Cxt A. We found that during periods where there was a detected sequence, surprisingly, animals froze significantly less than when outside a detected sequence epoch (**Figure 4B; Supplemental Figure 9;** Paired t-test: t=-3.25, p=0.0473**)**. This behaviorally-relevant feature of astrocytic sequences suggests further that these events are memory-specific in nature and that astrocytes are likely necessary for the maintenance of fear, in line with previous work[11,12,26–28].

Next, to determine if these cells form a stable substrate of memory, we aimed to uncover whether the reactivated cells in animals re-exposed to Cxt A preserved a stable, enduring pattern across different days. Earlier we noted that neither the proportion of reactivated cells across days nor the total number of

active cells during individual sessions were significantly different across groups (**Figure 1G-H**). Since we failed to find any differences in these metrics, we wanted to analyze how these cell populations might differ during a true recall session or a novel context exposure. To do this, we repeated our prior analysis (**Figure 2D; 3H-I**) and plotted cross validated heatmaps of only the reactivated cells (**Figure 4D; Supplemental Figure 10**). However, as opposed to sorting Odd events on the Even events, we instead plotted the heatmap by using the true peak times of the reactivated cells in the Cxt A or Cxt B session, and then plotted the same heatmap using the peak times obtained from CFC. We found a striking difference in these heatmaps, noting a far more structured sequence in the Cxt A heatmaps **(Figure 4D; Supplemental Figure 10)**. To quantify this, we then calculated the Spearman's correlation coefficient between the recall peak times, and the cross-validated peak times, finding a significant correlation in all Cxt A animals (**Supplemental Statistical Table**; one animal was excluded for having few reactivated cells). We found no significant correlations in Cxt B animals (**Supplemental Statistical Table**). Lastly, we tested if the Spearman's correlation coefficients from Cxt A were significantly different than Cxt B and found that indeed Cxt A was significantly more correlated than Cxt B (**Figure 4C;** Independent t-test: t=6.37, p=0.003). Together, these results suggest that astrocyte sequences are related to memory processes at both the cellular and behavioral level.

Discussion.

Our findings show that astrocytes generate robust, temporally-compressed calcium event sequences during both the acquisition and retrieval of contextual fear memory, resembling the properties of hippocampal time cells. We demonstrate that these astrocyte sequences in dCA1 are triggered by foot shocks during fear conditioning, they appear from the first shock on and reappear spontaneously during context-specific memory recall. Notably, these recall sequences are sustained by a stable population of reactivated astrocytes in mice exposed to Cxt A but not Cxt B, underscoring their context-specific nature. These sequences persist across days, maintaining their sequential structure during spontaneous fear memory recall. Finally, we establish the feasibility of using 1p imaging to track astrocytes in freely moving mice over multiple days, and, to our knowledge, this is a first in the field and permits largescale and longitudinal imaging of their activity across a variety of behaviors.

These findings are exciting in that our framework could be used to further analyze previous work. For example, a recent study established that hippocampal astrocytes ramp their activity in response to expected reward[8]. The authors show that the mean concurrent calcium events increase prior to reward, and we speculate that embedded within their observed activity are sequences encoding temporal features predictive of receiving a reward. Other work has also shown that position across a linear track can be decoded from hippocampal astrocytes akin to hippocampal place fields[7]. Curiously, the authors detect sequential like activity across the linear track, that ramps in response to reward, a phenomenon noted in canonical hippocampal time cells and akin to the prior mentioned study[6–8]. These exciting possibilities warrant future research investigating how the sequential structure of astrocytic activity contributes to the behavioral expression of memory.

What role do astrocyte sequences play in behavior and cognition? Perhaps the most provocative possibility is that these astrocyte cell sequences encode temporal context information in a way that is like canonical hippocampal time cells. The statistical features of the sequences (e.g., temporal-compression) we detected are in line with this result[19]. However, there are also features of these sequences which do not align with this model; for example, neuronal time cells have been found to persist on timescales much longer than tens of seconds, as we observed in the present study[29]. This discrepancy may be attributed to our methodological paradigm, as we utilized one-photon calcium imaging, which has lower resolution compared to two-photon microscopy, potentially limiting our ability to fully resolve astrocytic populations or understand how astrocytic subdomains may uniquely contribute. Moreover, current pipelines for neuronal ROI identification in calcium imaging experiments often perform sub-optimally for astrocytes, especially when focusing on somatic-specific events. To circumvent these issues, we manually segmented cells based

on their morphology and prominent somatic events, which led to the successful longitudinal imaging of several hundreds of astrocytes in awake behaving rodents.

Another potential biological role of these sequences is that astrocytes are necessary for the proper recall and storage of memory traces. In our study, we found that the sequences in recall sessions were related to the level of freezing of the animals. This dovetails with prior work from our group and others, which has demonstrated that astrocytic calcium events are associated with specific behavioral epochs[11,12,22–25]. This growing body of literature suggests that astrocytes are indeed relevant to behavioral outcomes, and highlights the need for more detailed, mechanistic investigations in future research. One possible explanation for this is that astrocytes work in tandem with hippocampal time cells to generate stable sequences necessary for the proper recall and anticipatory aspects of memory. Given recent research showing that hippocampal astrocytes mediate neurotransmitter signaling[30,31], it is plausible that astrocytes relay sensory information to dCA1 pyramidal cells, ultimately contributing to the generation of time cells.

Astrocytes are believed to promote plasticity-related mechanisms that support memory. Astrocytes form intimate contacts with neurons at the tripartite synapse via their peri synaptic astrocytic processes that are highly enriched with receptors and transporters that precisely modulate neurotransmitter functioning and homeostasis[32,33]. This privileged position allows astrocytes to perform or support some fundamental aspects of synaptic plasticity that are required for processing contextual and fear related information in dCA1[26,34]. Their ability to modulate plasticity could enable them to interact at synapses to form and modify the neuronal ensembles that are canonically understood to be the substrate of memory. Specifically, their coordinated bouts of activity during recall could enable the modification or updating of the synaptic strengths within these ensembles as mice learn that the environment is no longer aversive, or they may participate in forming new ensembles associated with extinction throughout the session[35]. This phenomenon has been described in areas including the basolateral amygdala, but the role of non-neuronal cells in the fine-tuning of neuronal ensembles during learning and memory is a burgeoning subfield of neuroscience[36–40].

To begin unraveling which of these mechanisms underly our findings, future work may include using higher resolution two-photon imaging of both astrocytes and neurons in regions like the hippocampus or amygdala to correlate astrocytic calcium dynamics with the formation and maintenance of coordinated ensembles. We selected one-photon imaging to enable naturalistic behavior across learning, but recent advances in freely moving two-photon technology would enable us to improve upon these findings with higher resolution imaging[41]. Further, recording both astrocytes and neurons at higher resolution would enable us to understand if and how astrocytes generate or sculpt temporal representations within the brain in parallel with neurons. Nevertheless, the context- and memory-specific nature of our findings provides a compelling foundation for future causal experiments.

Author Contributions. R.A.S., R.L.S., and S.R. conceptualized the experimental paradigm. R.A.S., R.L.S., and E.R. performed animal surgical procedures and calcium imaging experiments. R.A.S., R.L.S., R.C., E.R., and A.M. performed data analysis. M.D.B. performed behavioral analysis. R.A.S, R.L.S, and R.C. generated figures. R.C. performed the Bayesian Modeling. R.A.S, R.L.S, R.C., and S.R. wrote the paper. R.A.S., R.L.S., R.C., M.H., and S.R. interpreted the results and analysis. R.C. and M.H. provided expertise on temporal-sequence analysis.

Declaration of Interests. These authors declare no competing interests.

Data Availability Statement.
All raw data (e.g., original calcium imaging videos) and pre-processed data used to generate figures (e.g., CSV files) will be available upon reasonable request to the corresponding author.

Code Availability.
Code used in the current study is available at https://github.com/rsenne/dCA1_Paper.

Figures.

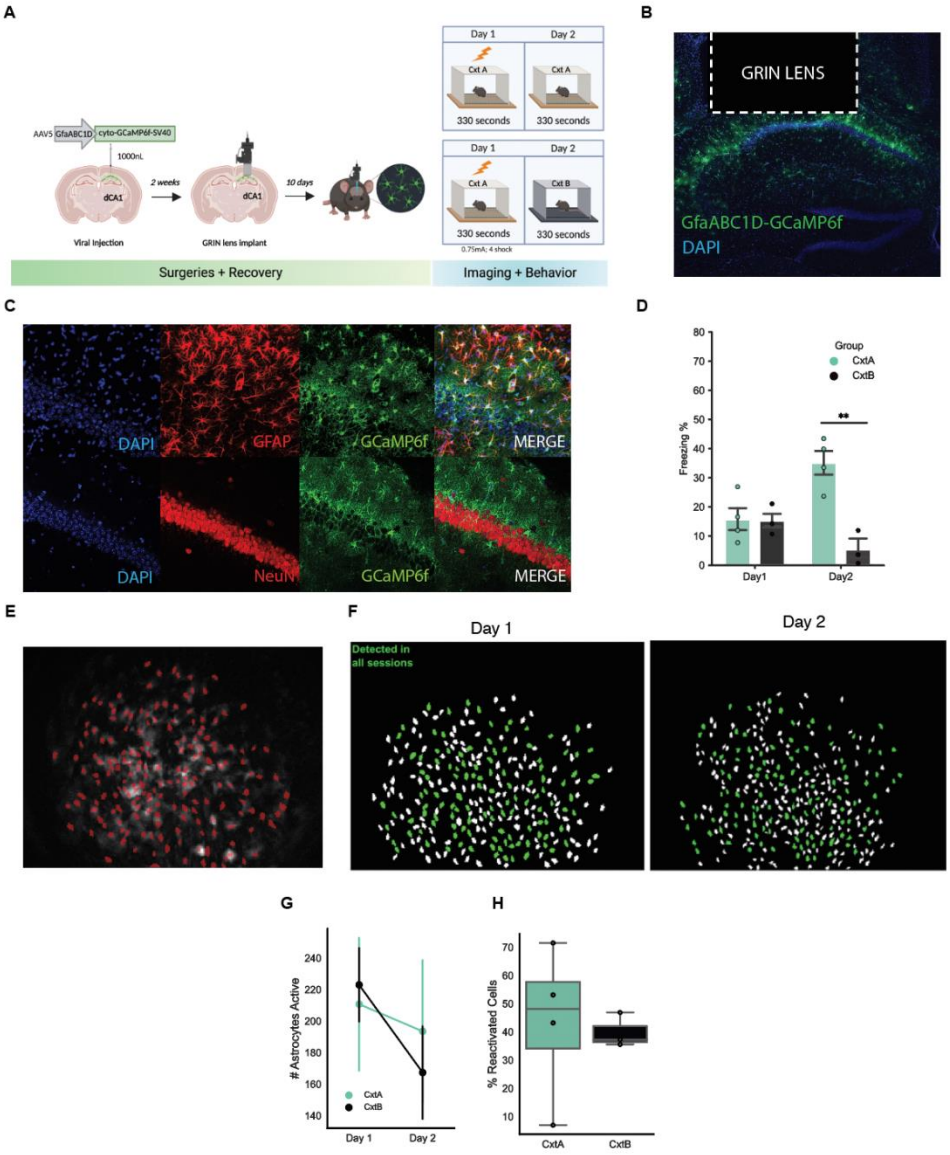

Figure 1: One-photon imaging of astrocytes in the dorsal hippocampus across contextual fear learning and recall.

(A) Astrocyte one-photon (1p) recordings in dorsal CA1 (dCA1) of the hippocampus. Wild type C57BL/6J mice were injected with 1000nl of the astrocyte-specific genetically encoded calcium indicator, AAV5-GfaABC1D-cyto-GCaMP6f-SV40, into dCA1 and allowed two weeks for recovery before implantation of a gradient-index (GRIN) lens above the pyramidal cell layer. After 10 days of post-surgical recovery, mice were imaged using the nVista System (Inscopix, Inc.). On Day 1, all mice (n=7) underwent contextual fear conditioning (CFC) for 330 seconds in Context A (Cxt A; blue throughout figure), where they received four foot shocks (0.75mA, 2s duration) at the 120, 180, 240 and 300 second time points. On Day 2, mice underwent a 330 second contextual recall session in the same mouse conditioning chamber (Cxt A) or were instead exposed to a novel Context B (Cxt B; orange throughout figure) for the same duration of time as a memory-specific control.

(B) Representative 20x confocal microscopy image of the dCA1 pyramidal cell layer expression of GfaABC1D-GCaMP6f (green; astrocytes) and DAPI (blue; nuclei) with an approximate location of the GRIN lens implantation.

(C) Representative 20x confocal microscopy images of the dCA1 pyramidal cell layer visualizing DAPI+ cells (blue; nuclei), GfaABC1D-GCaMP6f (green; viral expression), glial fibrillary acidic protein (GFAP) (red; astrocytes) or NeuN (red; neurons) to ensure selective expression of our virus in astrocytes.

(D) Average percent (%) freezing for Day 1 (CFC) and Day 2 (recall/novel exposure) across Cxt A and B groups shows both groups display similar levels of freezing on Day 1, and Cxt A mice freeze more during Day 2, as expected.

(E) Representative regions-of-interest (ROIs) map shows all astrocytes active during CFC from a mouse that were detected using manual ROI selection and curation.

(F) CellReg output that shows a representative set of tracked astrocytes across Days 1-2, where green ROIs are detected across both sessions.

(G) Number of astrocytes active on Days 1-2 across Cxt A and B groups indicates no significant difference in the total number of cells across days for either group.

(H) Percentage of 'reactivated' astrocytes (# reactivated astrocytes during Day 2/total # astrocytes during Day 1) across Cxt A and B groups shows no significant difference.

For 1D and 1G, Two-way RM ANOVA was performed with Sidak's multiple comparisons test (post-hoc) where applicable. For 1H, an independent t-test was performed. Significance was indicated by: *$p \leq 0.05$, **$p \leq 0.01$, ***$p \leq 0.001$, ****$p \leq 0.0001$. Error bars in all plots indicate mean ± SEM. All data was tested for normality and no outliers were removed. Cxt A (n = 4) and Cxt B (n = 3). See Supplemental Statistical Table for details.

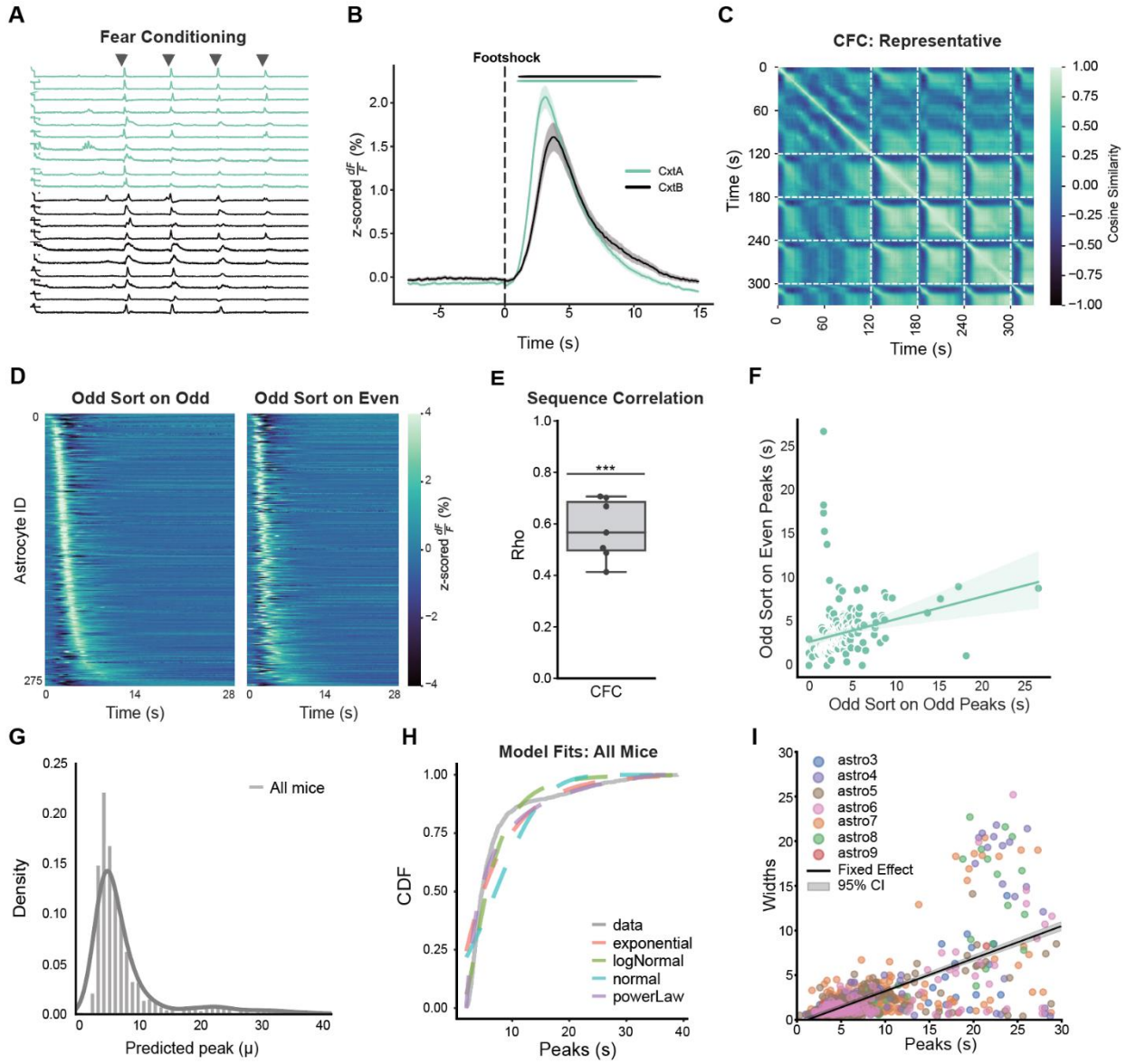

Figure 2: Evidence of astrocytic temporal sequences after foot shock onset.

(A) Representative calcium time series for Cxt A (blue) and Cxt B (black) showing almost all astrocytes display a robust response to one or more shocks during the contextual fear conditioning (CFC) session.

(B) Peri-event analysis for astrocytes in Cxt A (blue) and Cxt B (orange) show increased activity on average (z-scored % dF/F) at the time of each 0.75 mA foot shock (dashed line; 120, 180, 240, 300s). Shock response is averaged for each group with Cxt A (n = 4) and Cxt B (n = 3). Here, we used a 95% t-confidence interval (tCI) method where a significant event is indicated by the colored bars above the time series. These intervals indicate any time >1.0 seconds that did not include the mean-shifted baseline of 0.

(C) Representative cosine-similarity plot of each pair of astrocytes in time for an animal (Astro4). Here, we observe block-like structured activity after the onset of the first foot shock across all mice during CFC. Dashed white lines indicate the times of administered foot shocks (120, 180, 240, and 300s).

(**D)** Representative heatmap of all astrocytic calcium activity for an animal (Astro4) (z-scored % dF/F) that was averaged across shocks #1 and 3 (Odds) and sorted by their argmax during CFC. Time = 0 indicates the onset of each foot shock. To assess the stability of the sequential response, the same activity for Odds was sorted based on the argmax of the average response of each astrocyte to shocks #2 and 4 (Evens). Here, we observe a stable sequence across all animals across foot shocks (n = 7).

(E) Spearman's correlation between the true peak times (Odd sorted on Odd) and the cross-validated peak times (Odd sorted on Even) shows a significant difference between the average rho value and the hypothesized value of zero (n = 7) (One-sample t-test: t=13.19, p<0.0001).

(F) Representative linear regression of the true peak times (i.e., Odd Sort on Odd Peaks against the cross-validated peak times (i.e., the Odd Peaks sorted on the Even Peak times) for an animal (Astro4) (slope=0.256; intercept=2.71; p_value_slope=0.00017; p_value_bias=3.73E-21; R^2=0.065).

(G) Density histogram and kernel density estimation plot of predicted peak times (μ) at the population level (n = 7) show a skewed distribution after the onset of foot shock on average.

(H) Plots of the empirical cumulative distribution function and the theoretical cumulative distribution functions (CDFs) of the fit models (i.e., Power-Law (purple; WAIC= 7879), Exponential (red; WAIC=8837), Gaussian (teal; WAIC=9854), Lognormal (green; WAIC=8015), Actual Data (grey). Power-Law is the best fit for our data, indicating temporally compressed structure. Kolmogorov-Smirnov (K-S) test for Power-Law shows that even the best fitting model does not perfectly capture the peak distribution (KS distance = 0.46, p<0.001).

(I) Scatter plot of the within-trial time field width (σ) as a function of the peak location (μ) for each astrocyte from all mice. Here, the width of a calcium event (individual data points shown) increases linearly with time after foot shock (peak location) as determined by a linear mixed effects model. The solid line indicates the fixed effects best fit line that predicts Y from X with the associated 95% CI are shown on the plot (slope = 0.364, p<0.001).

Significance was indicated by: *p ≤ 0.05, **p ≤ 0.01, ***p ≤ 0.001, ****p ≤ 0.0001. All data was tested for normality and no outliers were removed. All mice (n = 7). See Supplemental Statistical Table for details.

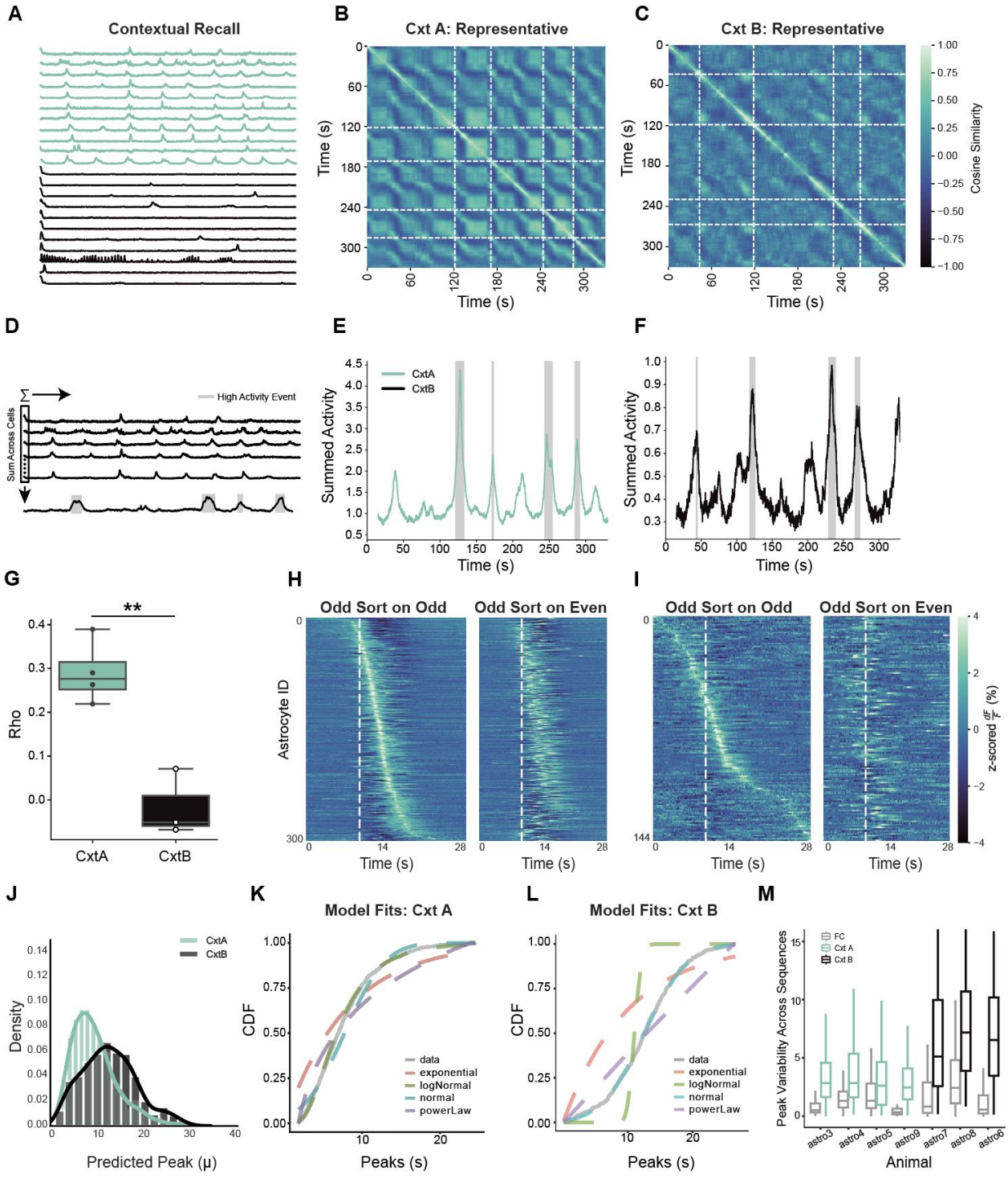

Figure 3: Astrocytes maintain a context-specific sequence structure during memory recall.

(A) Representative calcium time series for Cxt A (blue) and Cxt B (black) showing qualitatively distinct astrocytic calcium activity profiles, with Cxt A mice displaying more events when placed back into the conditioned context vs novel exposure in Cxt B.

(B-C) Representative cosine similarity plots for a Cxt A **(B;** Astro4) and Cxt B **(C;** Astro7) mouse, showing that mice re-exposed to Cxt A had more temporal structure in their astrocytic calcium than Cxt B. Dashed lines indicate the detected high-activity events described in (D).

(D) Spontaneous event detector graphic; individual astrocytic calcium activity was summed over each time index to generate a summed activity trace for a given mouse. Temporal thresholding was performed by finding the time indices where the summed activity was > 1.5 standard deviations above the mean and lasted for > 1 second. These time periods qualified as a detected 'event' that likely correlated with high activity seen during sequences (grey).

(E-F) Representative summed activity traces for a Cxt A **(E;** Astro4) and Cxt B **(F;** Astro7) mouse showing the detected spontaneous calcium events in grey. Although high activity events were detected across both groups, the characteristics of this activity across groups are explored below.

(G) Boxplot of Spearman's Rho values for each group. Correlations were calculated on the true peak times (Odd sorted on Odd) and cross-validated peak times (Odd sorted on Even). Points represent individual animals (Independent t-test: t=5.44, p=0.002834).

(H-I) Representative heatmaps of astrocytic calcium activity. **(H)** Left: Averaged heatmap of odd spontaneous detected events sorted by the argmax of peak times from odd events of an animal (Astro4) re-exposed to Cxt A. Right: Averaged heatmap of odd spontaneous detected events sorted by the argmax of peak times from even events. **(I)** Left: Averaged heatmap of odd spontaneous detected events sorted by the argmax of peak times from odd events from an animal (Astro7) exposed to Cxt B. Right: Averaged heatmap of odd spontaneous detected events sorted by the argmax of peak times from even events.

(**J)** Density histograms and kernel density estimation plots of predicted peak times (μ) at the population level for Cxt A (blue; n = 4) and Cxt B (black; n = 3) during recall show qualitatively unique distributions across groups.

(K) Empirical cumulative distribution function of the predicted peak times of animals re-exposed to Cxt A and theoretical cumulative distribution functions for fitted Exponential (red; WAIC=4811), Log-Normal (green; WAIC=4318), Normal (teal; WAIC=4517), and Power Law (purple; WAIC=4560) distributions. Log-Normal provides the best description of the data, indicating a temporally compressed structure in Cxt A activity.

(L) Empirical cumulative distribution function of the predicted peak times of animals exposed to Cxt B and theoretical cumulative distribution functions for fitted Exponential (red; WAIC=3548), Log-Normal (green; WAIC=3332), Normal (teal; WAIC=3101), and Power Law (purple; WAIC=3292) distributions. The Normal distribution provides the best description of the data.

(M) Boxplot of standard deviation of estimated peak locations across sequences in fear condition (grey), Cxt A (blue) and Cxt B (black), separated by animals. Lower value indicates the cell consistently peaks at the same time after the sequence onset. The bar in the middle indicates the median for the group (Independent t-test, t = 5.87, p=0.025).

Significance was indicated by: *p ≤ 0.05, **p ≤ 0.01, ***p ≤ 0.001, ****p ≤ 0.0001. All data was tested for normality and no outliers were removed. Cxt A (n = 4) and Cxt B (n = 3).

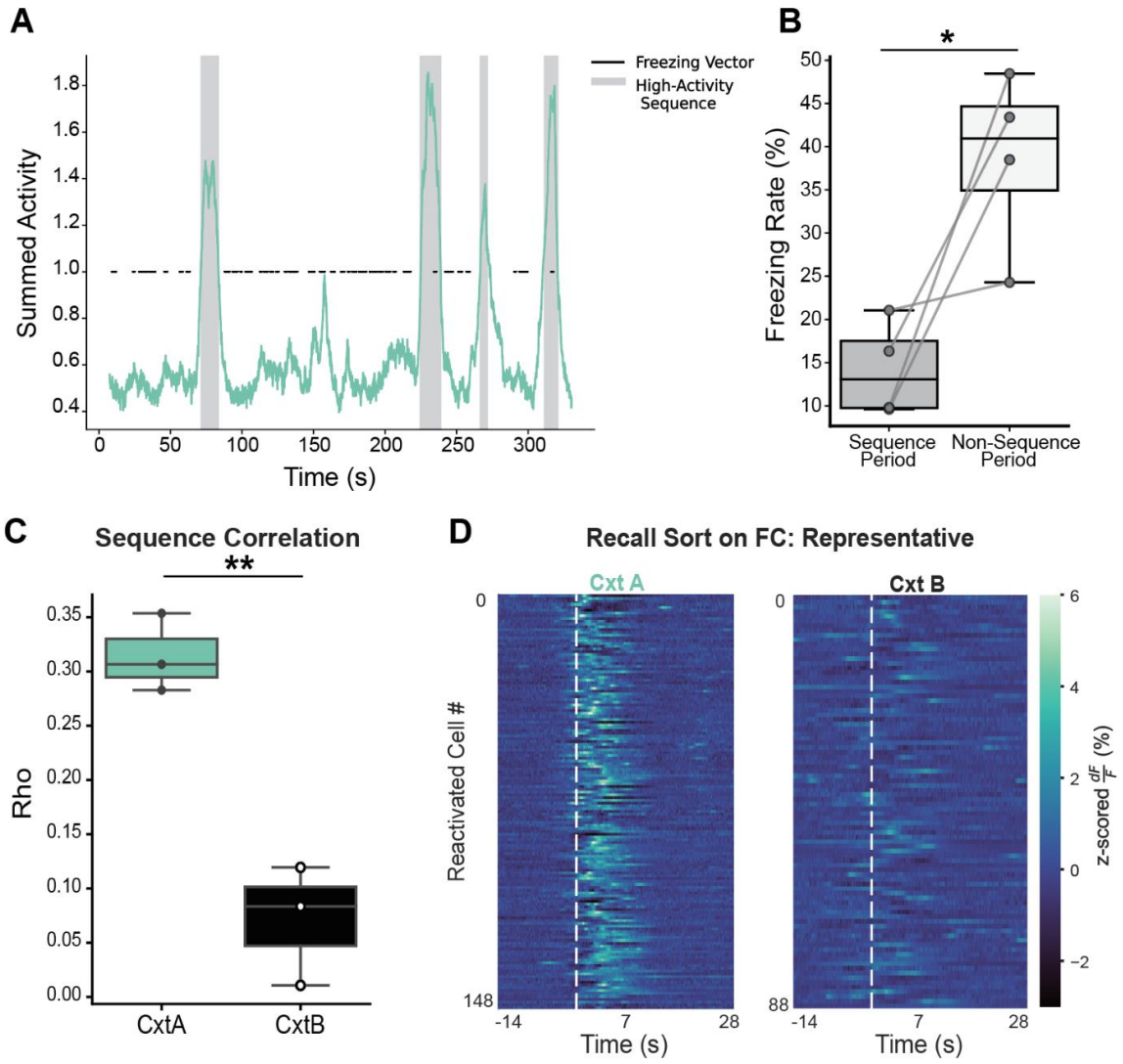

Figure 4: Reactivated astrocytes maintain sequential structure during memory recall

(A) Representative summed activity trace for an animal in Cxt A during recall showing an inverse relationship between detected epochs of high activity (grey) and freezing periods (black).

(B) Quantification of the average percent freezing in Cxt A animals (n = 4) during high activity 'sequence' periods compared to 'non-sequence' periods. Cxt B mice were not included in this analysis as they did not freeze during recall (*see Figure 1D; Supplemental Figure 1B*). During sequence periods, Cxt A animals froze significantly less than when outside a detected sequence (Paired t-test: t=-3.25, p=0.0473).

(C) Spearman's Rho values for each group during recall. Correlations were calculated for the 'reactivated' cells (e.g. astrocytes that were present across days), between their peak time on average during fear conditioning (FC) at the times of foot shock (FC Sort on FC; not shown, see Supplemental Figure) and the cross-validated peak times on average at the time of spontaneously detected high activity events (Recall Sort on FC). Points represent individual animals (Independent t-test: t=6.37, p=0.003107).

(D) Representative heatmaps of calcium activity from 'reactivated' astrocytes in Cxt A (left; Astro5) and Cxt B (right; Astro7), sorted by their ordering in the foot shock sequence during FC (Recall Sort on FC).

Significance was indicated by: *p ≤ 0.05, **p ≤ 0.01, ***p ≤ 0.001, ****p ≤ 0.0001. All data was tested for normality and one animal (Astro9) was removed from the Cxt A group due to having a low number of reactivated cells (**4B-C**; *data from this animal is shown in Supplemental Figure*). Cxt A (n = 4) and Cxt B (n = 3).

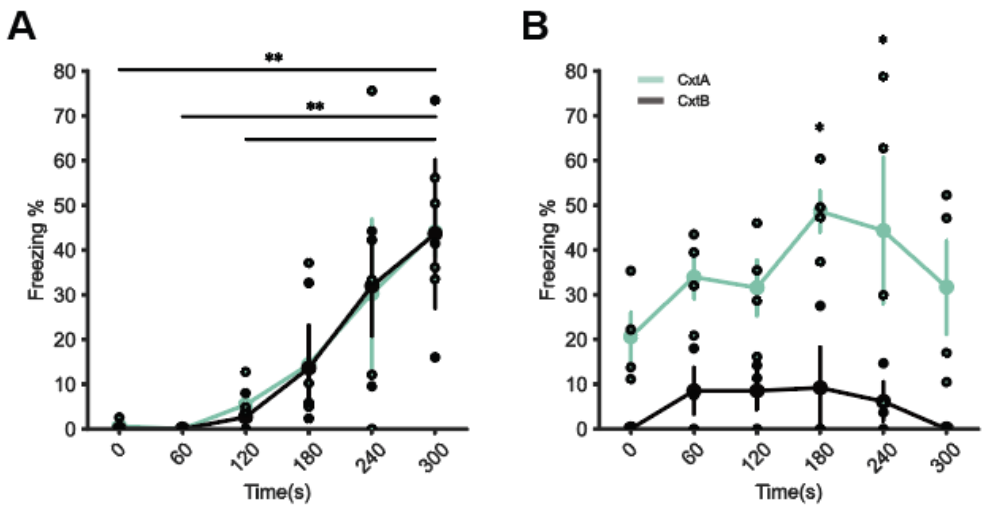

Supplemental Figure 1: Fear conditioning and recall freezing across time.

(A) Freezing percentage across contextual fear conditioning (CFC) 1-minute time bins indicate that mice in Cxt A (blue) and Cxt B (black) acquired fear at similar rates, as expected. Significant main effect of Time (Mixed-effects model (REML); [Time x Group] F(5,12) = 0.04285, p = 0.1948; [Time] F(5,18) = 7.242, p = 0.0007; [Group] F(1,5) = 0.008831, p = 0.09267). This was driven by significant differences in freezing levels across time bins in both groups (Sidak's multiple comparisons: [Cxt A] 0 vs 300s, p = 0.0067; 60 vs. 300s, p = 0.0057; 120 vs. 300s, p = 0.0215. [Cxt B] 0 vs. 300s, p = 0.0145; 60 vs. 300s, p = 0.0148; 120 vs 300s, p = 0.0256).

(B) Freezing percentages across contextual recall in 1-minute time bins indicate that mice in Cxt A froze significantly more than Cxt B, because they were re-exposed to the fearful context. Significant main effect of Group when freezing was analyzed across time within the recall session (Two-way RM ANOVA; [Time x Group] F(5,25) = 0.5339, p = 0.7485; [Time] F(5,25) = 1.478, p = 0.2324; [Group] F(1,5) = 25.76, p = 0.0039; [Subject] F(5,25) = 1.742, p = 0.1618). Post-hoc multiple comparisons revealed this effect was driven by significant differences at the 180 and 240s time bins (Sidak's multiple comparisons [Cxt A vs. B]: 180s; p = 0.0109, 240s; p = 0.0144). Error bars in all plots indicate mean ± SEM. All data was tested for normality and no outliers were removed. Cxt A (n = 4) and Cxt B (n = 3). Significance was indicated by: *p ≤ 0.05, **p ≤ 0.01, ***p ≤ 0.001, ****p ≤ 0.0001.

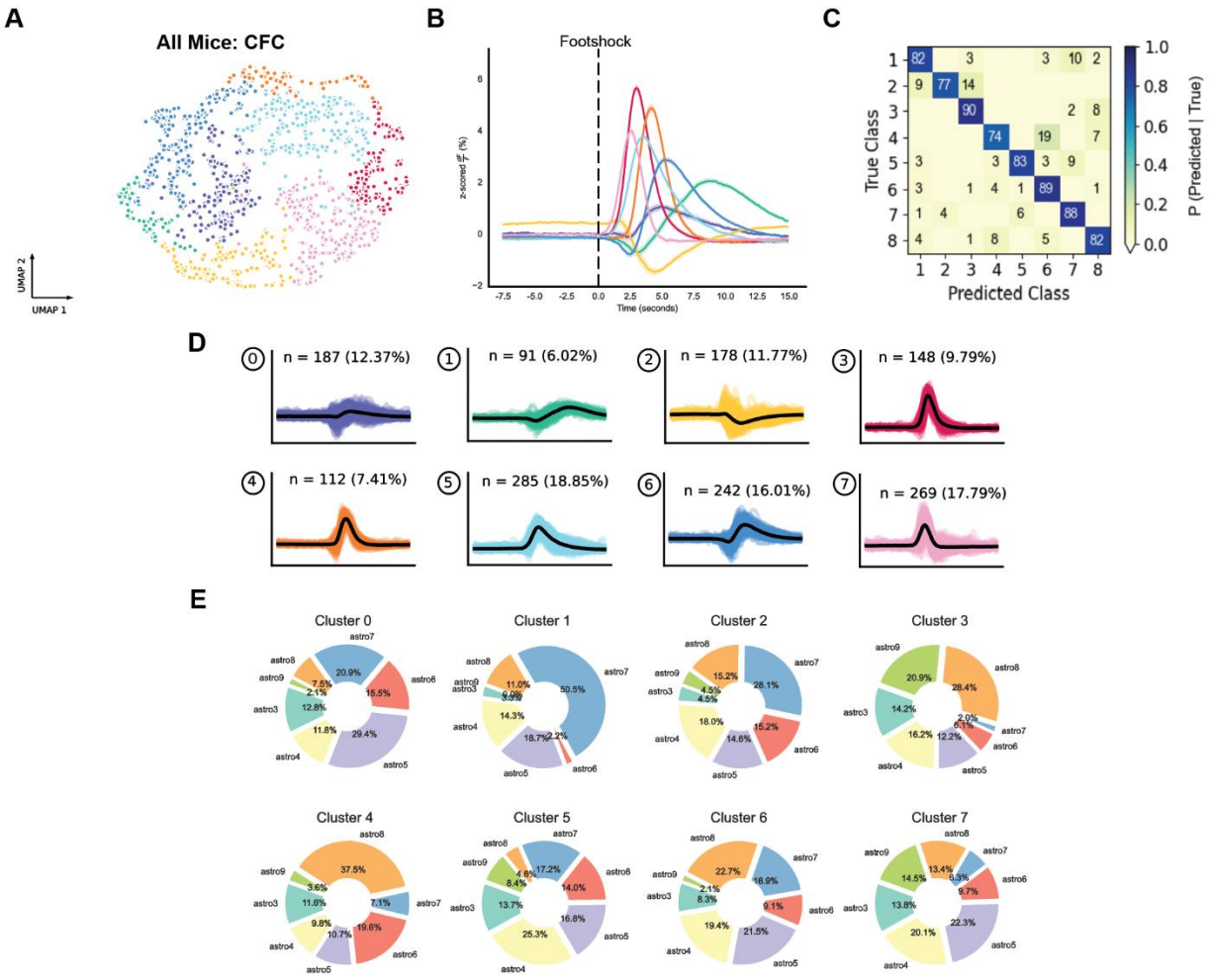

Supplemental Figure 2: Exploratory investigation of astrocytic calcium dynamics in response to foot shock using WaveMAP.

(A) WaveMAP results for all mice during CFC represented in two-dimensional UMAP space. The colormap is matched across all parts of the figure to represent each cluster.

(B) Average foot shock response (z-scored % dF/F) for each of the 8 clusters detected by WaveMAP, displaying temporal characteristics.

(C) Confusion matrix displaying high accuracy in correctly classifying calcium waveforms within their respective cluster. These matrices were used to optimize WaveMAP parameters that would most accurately cluster astrocytic waveforms (n_neighbors=10; mindistance=0.1).

(D) Average calcium waveforms within each detected cluster (0-7). n values represent the number of astrocytes that fall within that cluster and what percentage of the total population is represented.

(E) Percentage of astrocytes for each animal represented within a respective cluster (0-7) show that clusters are not driven by individual animal differences. Colors here do not correspond to the cluster colors. See Supplemental Statistical Table and Methods for more details.

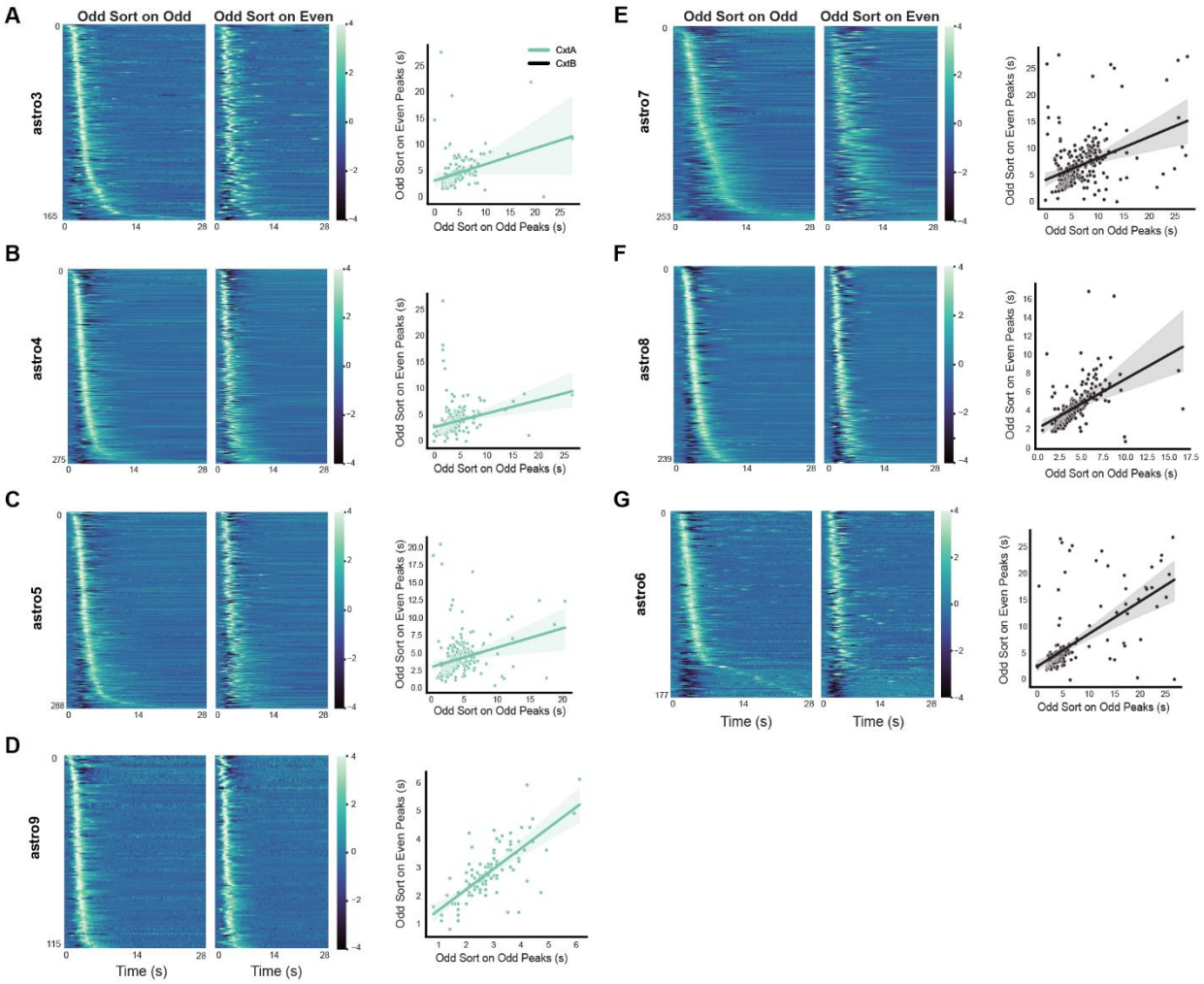

Supplemental Figure 3: Cross validated heatmaps for contextual fear conditioning.

(A-G; left) Heatmaps of all astrocytic calcium activity that was averaged across shocks #1 and 3 (Odds) and sorted by their argmax during CFC. To assess the stability of the sequential response, the same activity for Odds was sorted based on the argmax of the average response of each astrocyte to shocks #2 and 4 (Evens). Here, we observe a stable sequence across all animals across foot shocks (n = 7). Spearman's correlation calculated between the true peak times (Odd sorted on Odd) and cross-validated peak times (Odd sorted on Even) showed a significant difference between the average rho value (n =7) and zero using a one-sample t-test (*Figure 2F*).

(A-G; right) Linear regressions of the true peak times (i.e., Odd Sort on Odd Peaks) against the cross-validated peak times (i.e., the Odd Peaks sorted on the Even Peak times) for all animals. The solid line indicates the fixed effects best fit line that predicts Y from X with the associated 95% CI on each plot. See Supplemental Statistical Table for more details.

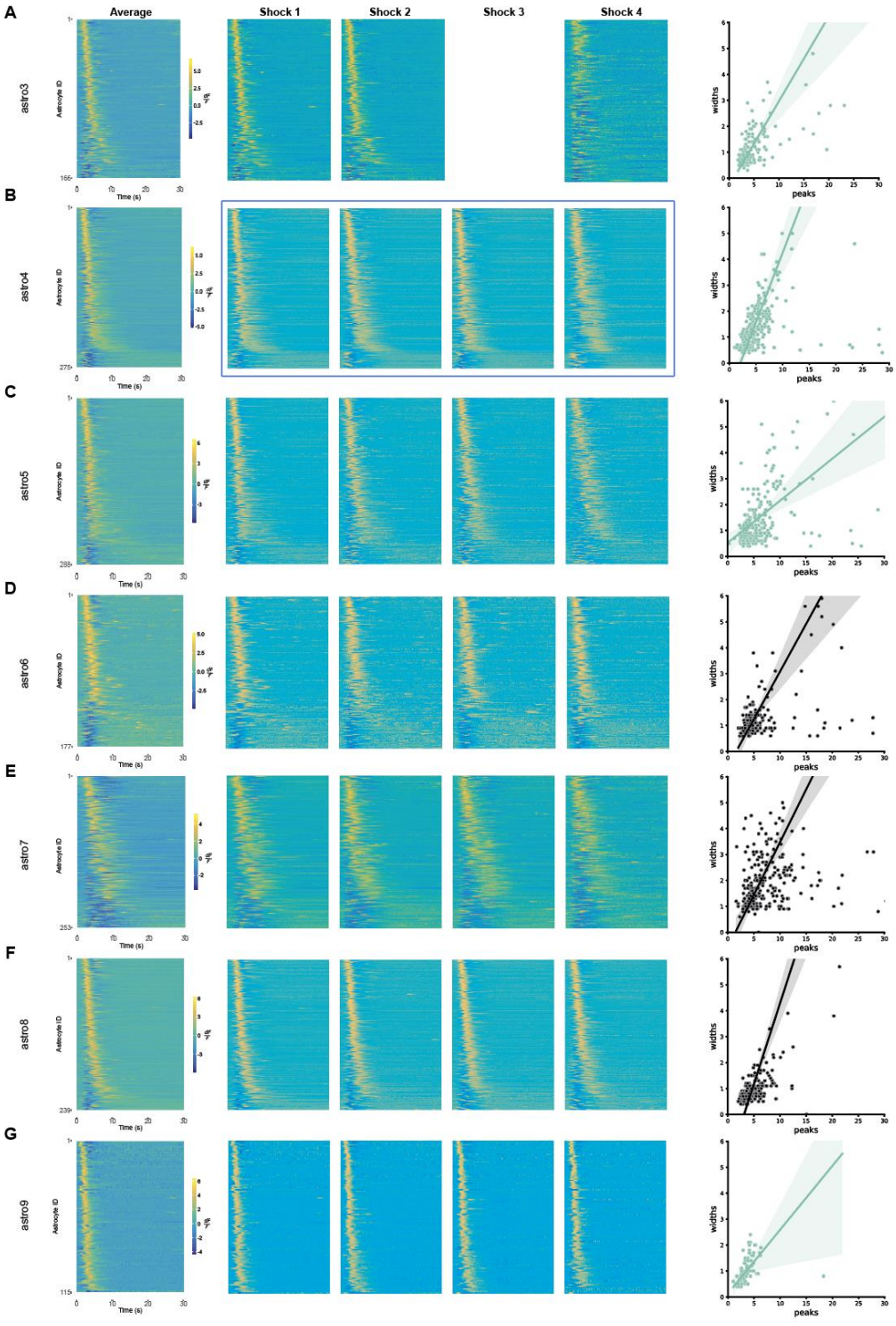

Supplemental Figure 4: Individual shock heatmaps for all animals derived from Bayesian model for contextual fear conditioning.

(A-G) Heatmaps of individual astrocytic calcium traces in response to foot shock for all mice: (A) astro3, (B) astro4, (C) astro5, (D) astro6, (E) astro7, (F) astro8, (G) astro9. Astro3 is missing the third shock, as the mouse avoided foot shock by propping itself up on the side of the chamber. These were sorted on the

predicted peak times (μ) that were extracted from the Hierarchical Bayesian Model. Lower values of mu (i.e., cells that had earlier peak times) are plotted on the top (i.e., ascending order). Average (left) and individual detected sequences (middle). Accompanying simple linear regressions (right), showing the within-trial calcium event width (σ) as a function of the peak location (μ) for each astrocyte. See Supplemental Statistical Table for details. Regression plots model the relationship between the individual receptive field widths (i.e., σ) against the peak locations (i.e., μ). All animals show a significant relationship between these values (*See Supplemental Statistics table*).

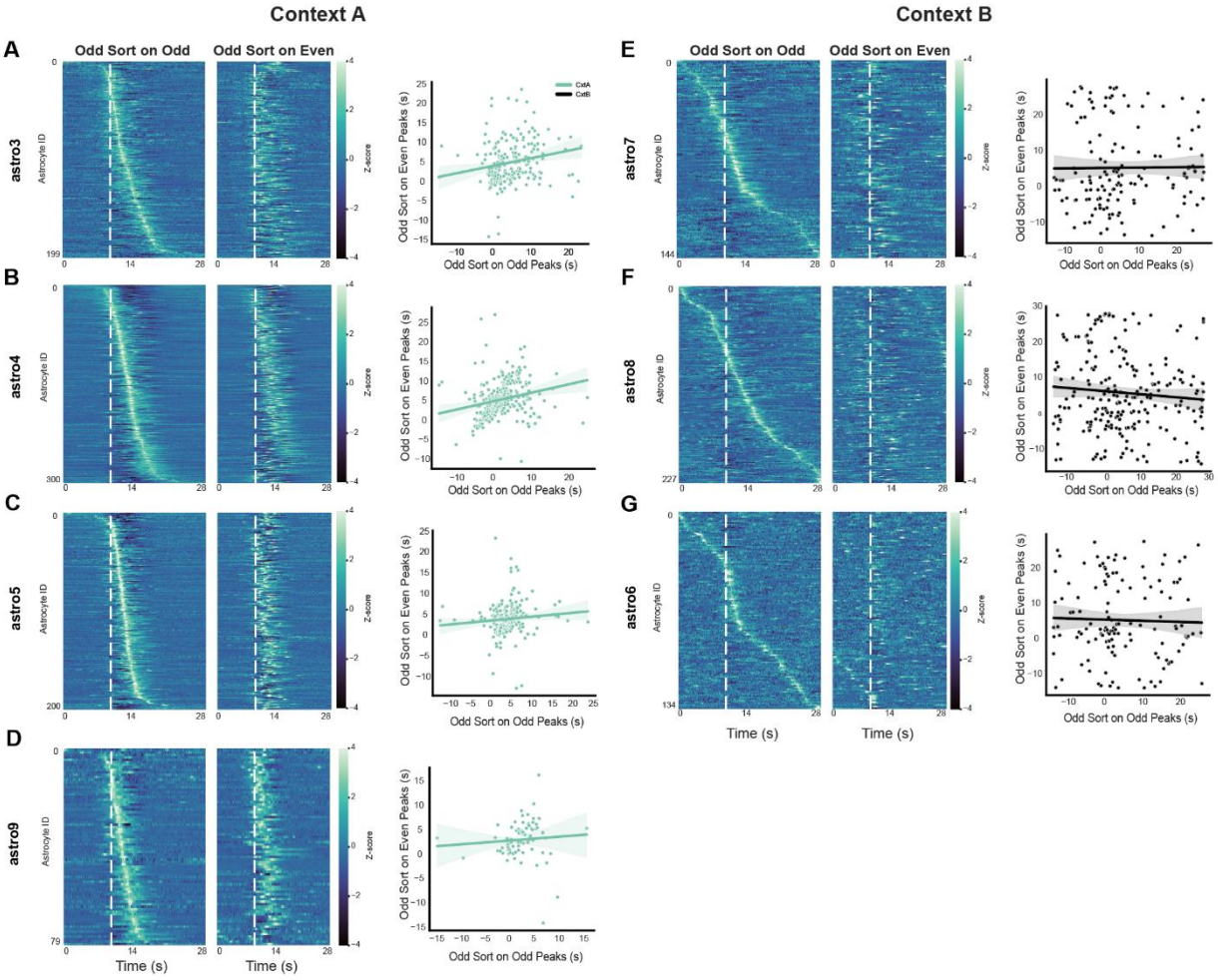

Supplemental Figure 5: Cross validated heatmaps for recall.

(A-G; left) Heatmaps of all astrocytic calcium activity that were averaged across spontaneously detected events #1 and 3 (Odds) and sorted by their argmax during recall. To assess the stability of the sequential response, the same activity for Odds was sorted based on the argmax of the average response of each astrocyte to spontaneously detected events #2 and 4 (Evens). Here, we observe a stable sequence across all animals in Cxt A (n = 4), but not in Cxt B (n = 3) during the recall session. Spearman's correlation calculated between the true peak times (Odd Sort on Odd) and cross-validated peak times (Odd Sort on Even) showed a significant difference between Cxt A and B groups (*Figure 3G-I*).

(A-G; right) Linear regressions of the true peak times (i.e., Odd Sort on Odd Peaks) against the cross-validated peak times (i.e., the Odd Peaks sorted on the Even Peak times) for all animals. The solid line

indicates the fixed effects best fit line that predicts Y from X with the associated 95% CI on each plot. See Supplemental Statistical Table for more details.

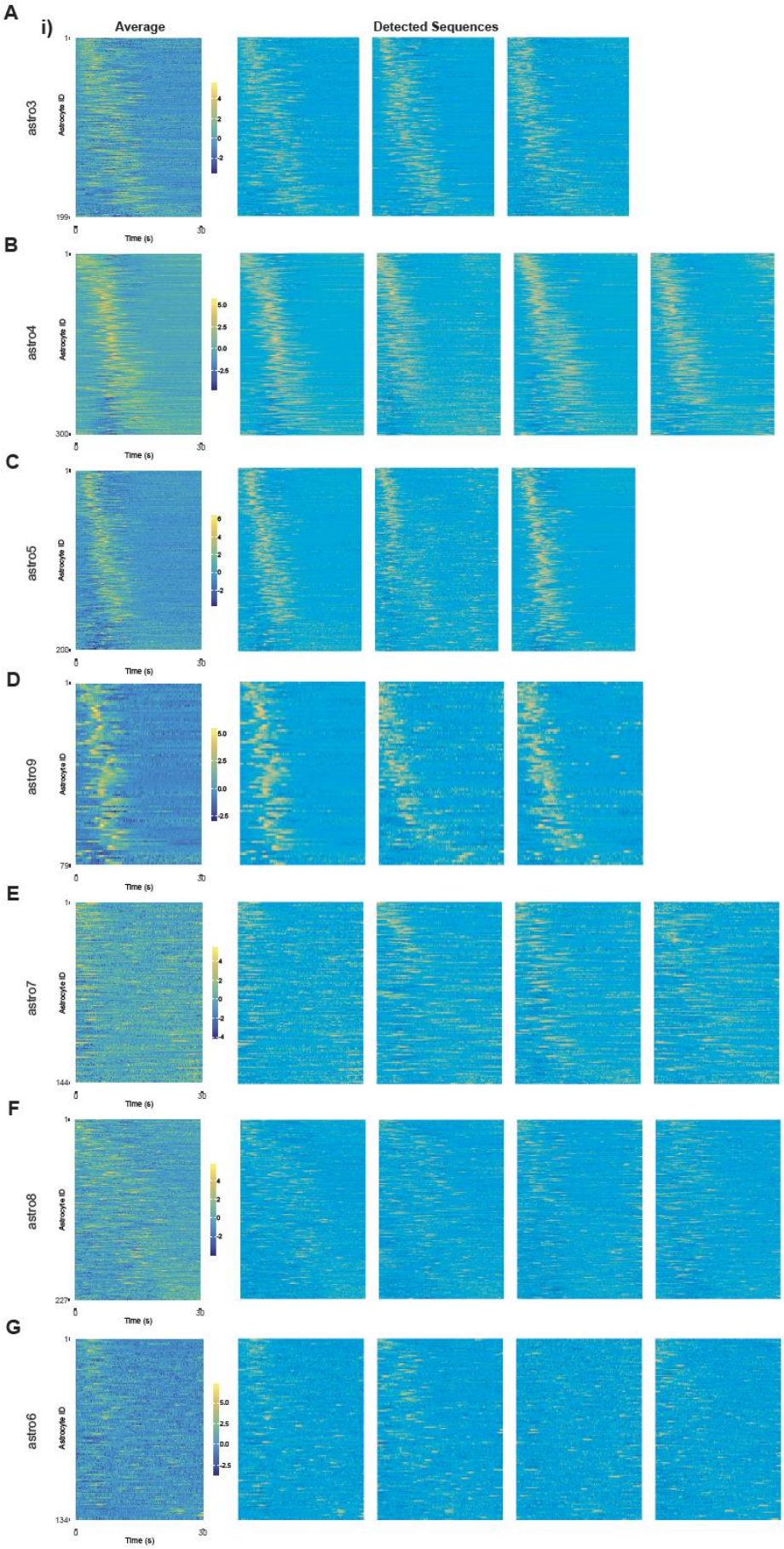

Supplemental Figure 6: Individual event detected heatmaps for all animals derived from Bayesian model during recall.

(A-G) Heatmaps of individual astrocytic calcium traces during detected sequences for all mice: **[Cxt A]** (A) astro3, (B) astro4, (C) astro5, (D) astro9; **[Cxt B]** (E) astro7, (F) astro8, (G) astro6. These were sorted on the predicted peak times (μ) that were extracted from the Hierarchical Bayesian Model. Lower values of mu (i.e., cells that had earlier peak times) are plotted on the top (i.e., ascending order). Average (left) and individual detected sequences (right). Cxt A (blue; n = 4) and Cxt B (black; n = 3).

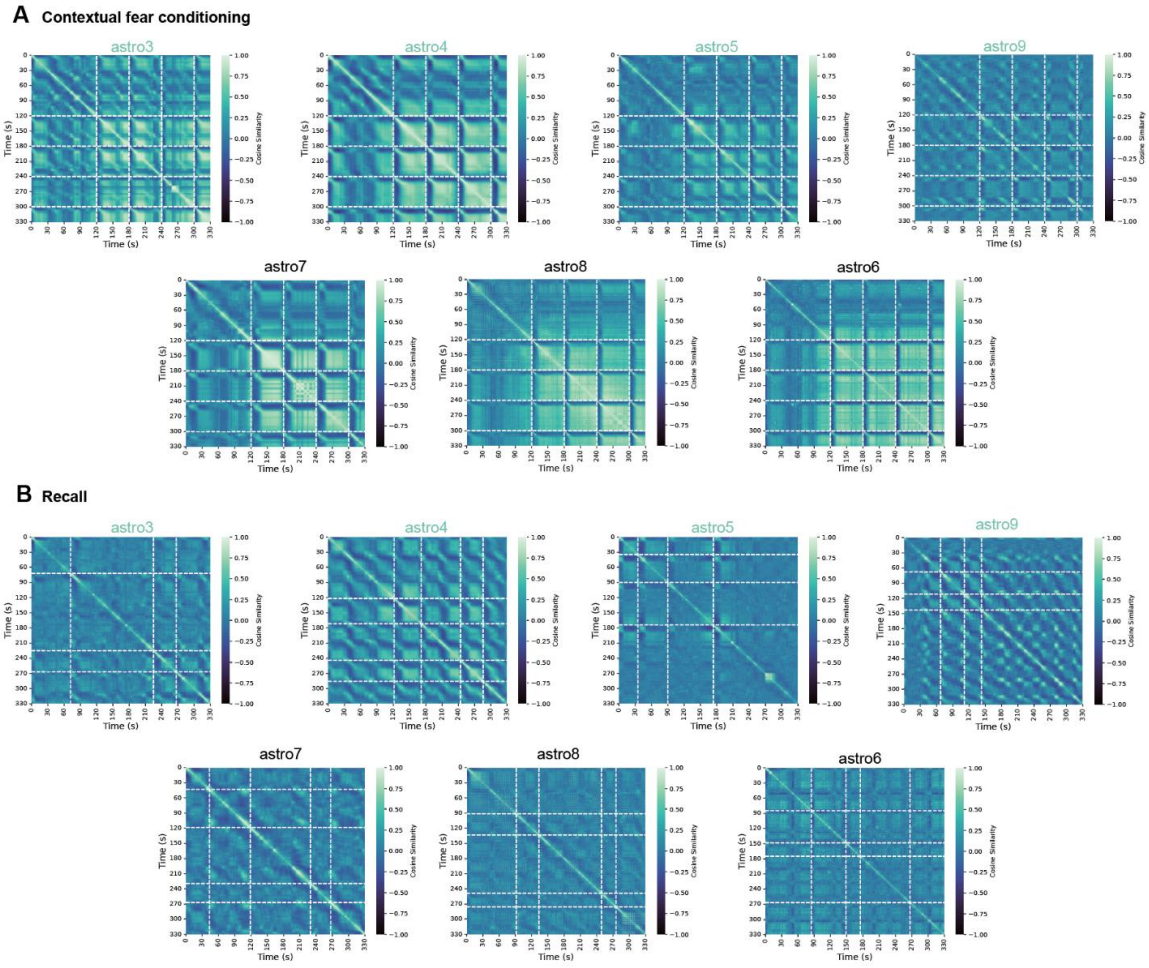

Supplemental Figure 7: Individual cosine similarity plots for fear conditioning and recall

(A) Cosine similarity plots for all animals (astro3-9) for contextual fear conditioning, showing the structured temporal dynamics induced by repeated foot shocks. Dashed lines indicate the times of administered foot shocks (120, 180. 240. 300 seconds).

(B) Cosine similarity plots for all animals (astro3-9) for recall, showing the structured temporal dynamics maintained in Cxt A (astro3, astro4, astro5, astro9), but not Cxt B (astro6, astro8, astro8) mice. Animal label colors (e.g. astro3) indicate Cxt A (blue) or Cxt B (black) groups. Dashed lines indicate the times of spontaneously detected events for each animal.

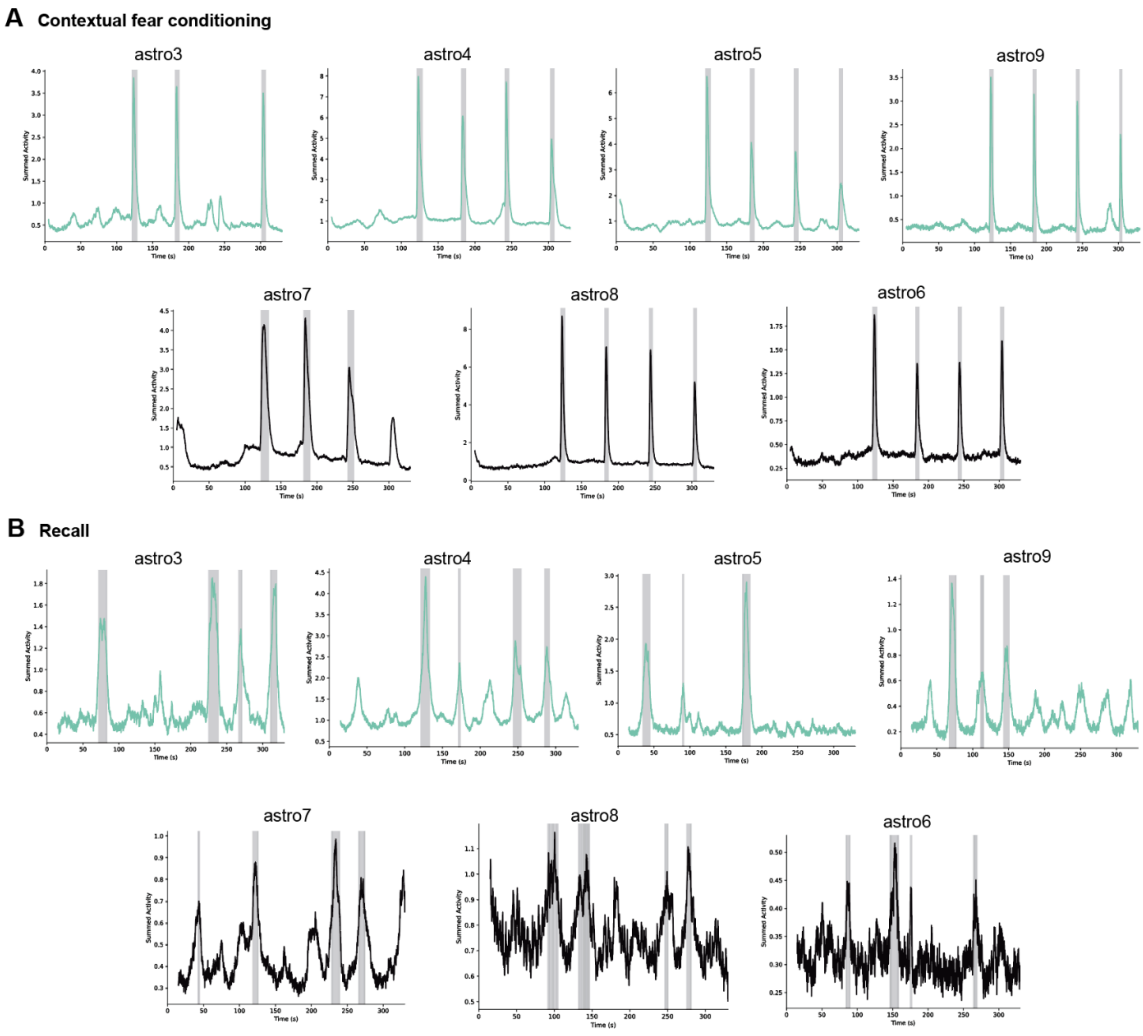

Supplemental Figure 8: Individual animal high-activity event detector results for contextual fear conditioning and recall.

(A) Detected shock sequences for all individual animals (astro3-9) during contextual fear conditioning as a confirmation of the 'sequence detector' described in *Figure 3*. Individual calcium activity was summed over each time index to generate the summed activity trace for a given mouse (solid line; Cxt A = blue, Cxt B = black). Temporal thresholding was performed by finding the time indices where the summed activity was > 1.5 standard deviations above the mean and lasted for > 1 second. These time periods qualified as detected 'sequences' (grey shading).

(B) Using the same method above, detected spontaneous sequences for all individual animals (astro3-9) during recall.

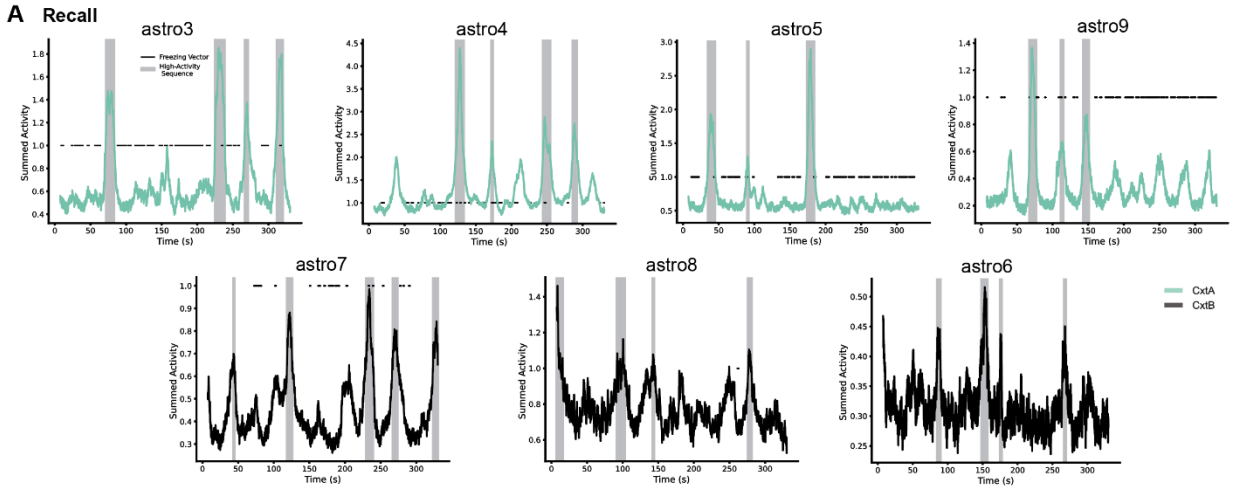

Supplemental Figure 9: Relationship of freezing epochs, summed activity traces, and spontaneously detected events.

(A) Summed activity trace for all animals in Cxt A (blue) and Cxt B (black) during recall, overlaid with detected epochs of high activity (grey) and freezing periods (black dashed lines). Animals in Cxt B froze at very low levels (e.g. astro6, astro7 and astro8). Animals in Cxt A showed an inverse relationship between detected epochs of high activity and freezing periods.

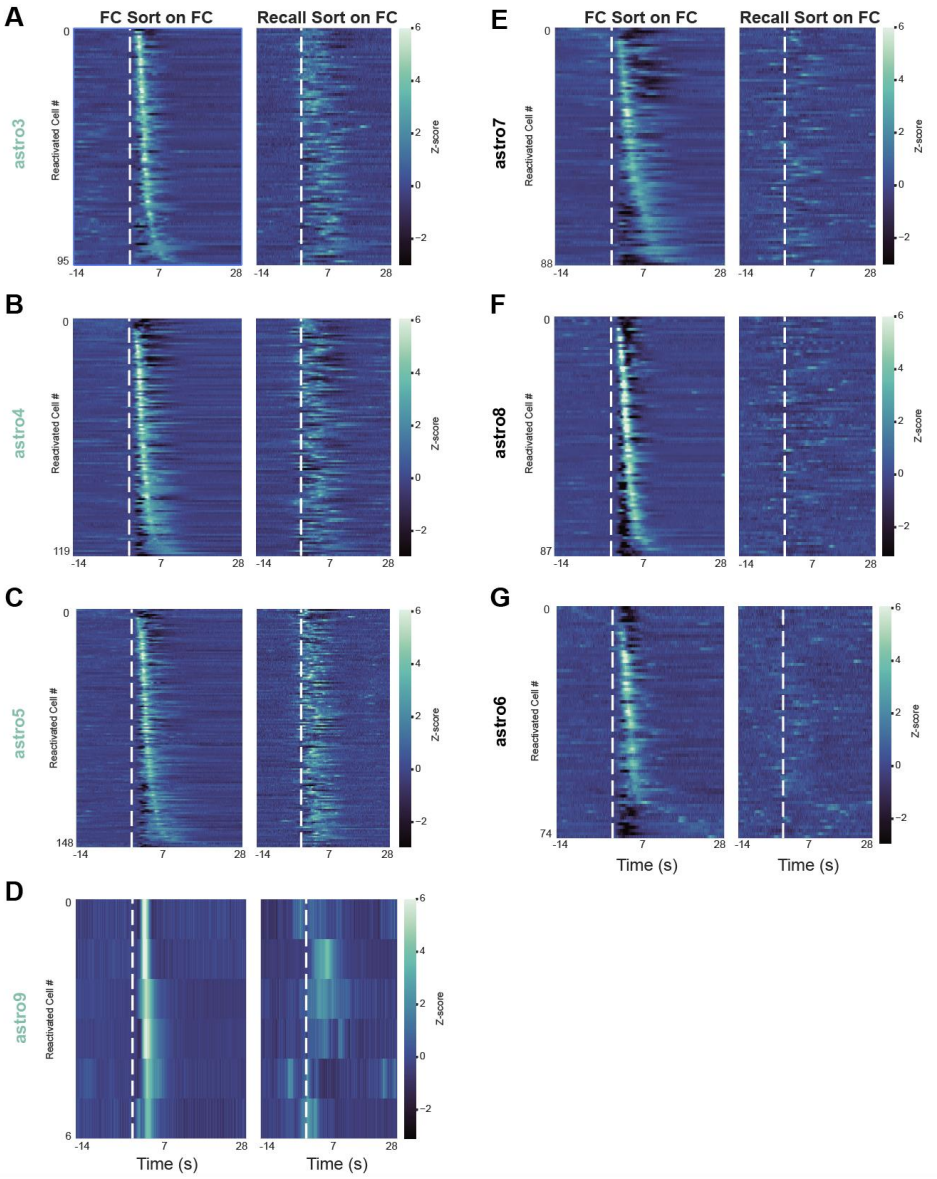

Supplemental Figure 10: Cross-validated heatmaps of recall session using only reactivated cells. **A-G)** *Left Panel:* Heatmap of cells in fear conditioning that were also present during recall sorted on the argmax of the peaks during shocks in fear conditioning. *Right Panel:* Heat map of the same reactivated cells averaged over spontaneously detected events, but, during re-exposure to Cxt A or exposure to Cxt B. Heatmap is sorted on the argmax values from FC. Animals who were re-exposed to Cxt A (e.g., sub panels A-D) show more sequence stability compared to animals exposed to Cxt B (e.g., E-G). Astro9 was removed from statistical analysis as it only had 6 'reactivated' cells.

Methods.

Subjects

The animals used in this study were male, wild-type C57BL6 (P29-35; 17-19g) mice obtained from Charles River Laboratories. Animals were housed in the Boston University animal facilities in standard ventilation cages on a 12:12 dark/light cycle (0700-1900) and given ad libitum access to standard food and water. Mice were housed with littermates in cages with 4-5 mice and after GRIN lens implantation, they were individually housed to prevent any damage to their implants. Following GRIN lens surgery, mice were given 10 days to recover before the start of behavior. All subjects were treated in accord with protocol 201800579 approved by the Institutional Animal Care and Use Committee (IACUC) at Boston University. No statistical methods were used to determine sample size but were instead based on sample sizes of previous 1p imaging studies.

Stereotaxic Surgery

Viral transduction: Mice were anesthetized with 3-3.5% isoflurane during induction and maintained at 2-3% inhalation using stereotaxic nose cone delivery (oxygen 1.2 L/min). Paralube ophthalmic ointment was applied regularly to the eyes to maintain adequate lubrication. Scalp hair was removed using Veet or Nair hair removal cream; this was subsequently removed using applications of betadine solution and ethanol (70%). Lidocaine hydrochloride (2.0%) was injected subcutaneously (SQ) as a local analgesic agent under the scalp prior to incision. Meloxicam (0.1mg/kg) was administered SQ at the start of surgery. After scalp incision, mice received a unilateral (right) craniotomy with a 0.5-0.6 mm drill bit for the dorsal hippocampal CA1 (dCA1) viral injection. A 10uL airtight Hamilton syringe with an attached 33-gauge beveled needle was used to inject AAV-GfaABC1D-cyto-GCaMP6f-SV40 (Penn Vector Core) at the coordinates of dCA1: -2.00 anteroposterior (AP), +1.40 mediolateral (ML) and -1.50 dorsoventral (DV). All coordinates are given relative to bregma (mm). 1000nL of undiluted virus was injected at 50nL/min using a micro infusion pump (UMP3; World Precision Instruments). After injection, the needle remained at the site of injection for 5-7 minutes to prevent viral spread. After injection, the incision was sutured closed using 4/0 Non-absorbable Nylon Monofilament Suture (Brosan). At the end of surgery, mice were injected with a 0.1mg/kg intraperitoneal (IP) dose of buprenorphine. Following surgery, mice were placed in a clean recovery cage with a heating pad until regaining reflexes. To allow time for viral expression and recovery, mice were monitored for 2 weeks prior to implantation of GRIN lens surgery.

GRIN lens implantation: After 2 weeks, we inserted a GRIN lens (Inscopix, Inc.). 30 minutes prior to surgery, mice were injected with 0.1mL of dexamethasone diluted in 0.1mL sterile saline IP to reduce brain swelling. Mice were prepared as described above and the previous incision site was reopened. A 0.5-0.6 mm drill bit was used to drill a 1 mm craniotomy around the previous site of injection at the coordinates listed above. Using vacuum suction, 30 to 34-gauge needle attachments and constant administration of cold, sterile saline, brain tissue was aspirated down just beyond the thick fibers of the corpus callosum. Blood control was performed using absorbable gelatin sponge (Surgifoam). A GRIN lens and integrated base plate were lowered slowly to -1.30DV and a biocompatible silicone adhesive (Kwik-Sil) was used to seal off the exposed perimeter of the lens and skull. Multiple layers of adhesive cement (C&M Metabond) were applied up to the cuff of the integrated base plate and the headcap was completed with darkened dental cement (Stoelting). Mice were administered the same doses of postoperative analgesics described above. They were able to recover for 10 days before imaging experiments were performed during our behavioral paradigm.

Behavioral testing

Prior to behavioral testing, all mice were handled and habituated to being plugged into the miniature microscope. On Day 1, mice were subjected to contextual fear conditioning (CFC) for 330s in Context A (Cxt A), where they received foot shocks (0.75mA, 2s duration) at the 120, 180, 240 and 300s time points.

On Day 2, mice underwent a 330s contextual recall session in the same mouse conditioning chamber (Cxt A) or were instead exposed to a novel Context B (Cxt B) for the same duration of time (330s).

Context parameters: Cxt A was a standard mouse conditioning chamber (18.5 x 18.5 x 21.5 cm; Coulbourn Instruments) with metal-panel side walls, plexiglass front and rear walls and a stainless-steel grid-floor (16 bars) that were connected to a precision animal shocker (Actimetrics). Cxt B was a standard mouse conditioning chamber of the same size in a different behavioral room that was modified to have striped plastic walls, almond scent, and a transparent plastic floor. No lighting differences or the presence of auditory stimuli existed in either context. Ethanol (70%) was used to clean Cxt A, while Rescue disinfectant spray was used to clean in Cxt B to maintain these odor profiles.

One-photon imaging.

Acquisition: All imaging experiments were conducted on awake, behaving mice in a freely moving manner in standard mouse conditioning chambers. GCaMP6f fluorescence signals were imaged using a miniature integrated fluorescence microscope system (Inscopix Inc.) with GRIN lenses implanted in the dorsal CA1 of the hippocampus (dCA1). Before the start of imaging, the miniature microscope was attached to the baseplate and adjusted to determine the best focal plane and gain for each mouse to achieve the best fluorescence signals. These values were maintained across all recording sessions. Frequency (Hz) and LED output power were consistent across all mice. Behavioral video was captured using the nVista Imaging System (Inscopix Inc.) that was triggered by an external TTL to time lock our behavioral session to calcium recordings (FreezeFrame4).

Pre-processing: Calcium imaging data were pre-processed using the Data Processing Software (Inscopix, Inc.; IDPS). Videos were cropped from 1280 x 800 pixels to 1200 x 800 pixels and spatially down sampled by a factor of 4, from 1200 x 800 pixels to 300 x 200 pixels and temporally down sampled by a factor of 2 from 20 to 10 Hz. A spatial bandpass filter was applied using the default settings in IDPS (low cut off: 0.005 and high cut-off = 0.500). Motion correction was performed with the first frame as the global reference frame origin. PCA-ICA and CNMFe analysis failed to identify individual astrocytes in a reliable manner. Thus, to identify individual cells, pre-processed images were converted to dF/F using the mean frame as a reference. Regions of interest (ROI)s were selected by manually identifying astrocytic cell bodies with high contrast over the session, and contours were drawn to contain the pixels of the somatic ROI. To validate this method, ROIs were further confirmed by visual inspection of the individual cell time series, and only those with clearly identifiable signals across two individual researchers were included in further analysis.

Longitudinal registration: Longitudinal cell ROI registration was performed using the open-source Matlab program, CellReg, that utilizes a probabilistic method for tracking cells across multiple sessions [10]. In brief, it first aligns each session field-of-view (FOV) to one another by projecting the centroid locations of all the cells' spatial footprints onto one image. It maximizes the cross-correlation between the projections of each session to the reference session (Day 1; fear conditioning). We utilized non-rigid transformations, as they best aligned our dataset. Next, the Pearson correlations between the spatial footprints of the pairs of neighboring cells were calculated, estimating the probability of them being the same cell across sessions (Psame) with a maximum distance of 13-14 um. Further, the data is modeled as a weighted sum of the two distributions (same and different cells), allowing for an estimate of the false-negatives and false-positives. Finally, Psame = 0.50 (default) was utilized as an input for a clustering algorithm. CellReg registered cell outputs were confirmed visually using custom Python scripts that allowed confirmation of proper cell pairs and generation of a csv file that contained the indices of each cell on Day 1 and 2, if applicable, with a value of -1 indicating the cell not being present on that day.

Behavioral analysis: Freezing behavior was scored using Any-Maze, allowing for identification of the onset, and offset of freezing epochs, as well as quantification of total percent time freezing (%) across the entire session or within defined time-bins (Stoelting Inc.).

Immunohistochemistry

After the completion of experiments, mice were overdosed with 3% isoflurane and transcardially perfused with cold phosphate buffered saline (PBS), followed by 4% paraformaldehyde (PFA) in PBS. Brains were extracted and placed in PFA at 4℃ for 24-48 hours. All brains were sliced coronally at 50um on a vibratome into cold PBS or 0.01% sodium azide in PBS for long term storage. Native green fluorescent (GFP) protein signal from the GCaMP6f expression was assessed and sections were counterstained for both astrocytes and neurons using immunohistochemistry (IHC).

For IHC, dorsal CA1 (dCA1) sections underwent three washes in PBS for 5-10 minutes each to remove the 0.01% sodium azide storage solution. Sections were washed in 0.2% Triton X-100 in PBS (PBST) for 3 x 5 minutes each at room temperature. Next, slices were blocked for 2 hours in 1% bovine serum albumin (BSA) and 0.2% Triton X-100 in PBS solution on a shaker at room temperature. Sections were incubated in primary antibodies (1:1000 mouse anti-GFAP [NeuroMab] or 1:500 polyclonal guinea anti-NeuN/Fox3 [SySy]; 1:1000 chicken anti-GFP) made in the same 1% BSA/PBS/Triton X-100 solution at 4C for 24-48 hours.

Sections underwent 3 x 5-minute washes in PBST to remove the primary antibody solution. Sections were incubated in secondary antibodies (1:1000 Alexa Fluor 555 goat anti-mouse IgG [Invitrogen] or 1:1000 Alexa Fluor 555 goat anti-guinea pig [Invitrogen]; 1:1000 Alex Fluor 488 goat anti-chicken [Invitrogen]) for 2 hours at room temperature on a shaker. Sections were washed 3 x 10 minutes in PBST, and subsequently mounted onto microscope slides (VMR International, LLC) with Vectashield HardSet Mounting Medium with DAPI (Vector Laboratories, Inc.). These were allowed to dry for 24 hours at room temperature and edges of the coverslips were clear nail polished to maintain moisture. Slides were stored in a slide box in 4C after imaging.

WaveMAP Clustering

Exploratory WaveMAP analysis of astrocytic calcium waveforms during contextual fear conditioning (CFC) were performed following the protocol described in Lee et al, 2021; 2023 and Supplemental Figure plots 2A, C and D were generated using code adapted from the WaveMAP_Figures_Data.ipynb Jupyter notebook (https://github.com/EricKenjiLee/WaveMAP_Paper). First, we compiled all single-astrocyte calcium traces from all animals (n = 7) during CFC and normalized the data via z-scoring. Next, for every trace, we generated an average shock response [120, 180, 240, 300 second time points] with a window of –7.5 seconds to 15 seconds after shock. Here, we concatenated these average shock responses for all animals into a numpy array that was fed into WaveMAP. This numpy array consisted of the time (column) and cell # (row) across all individual animals within CFC. Broadly, WaveMAP first normalizes the array by dividing each value by the maximum value in each row using NormWF. Next, it passes NormWF into UMAP to generate a high-dimensional UMAP graph. It further applies Louvain clustering to the graph and allows visualization of the detected clusters within UMAP space (**Supplemental Figure 2A**). The WaveMAP parameters were optimized and evaluated using a classifier's performance (**Supplemental Figure 2C**). Once the resulting clusters were optimally confirmed with the classifier, we examined all the individual cluster average waveforms and determined the total number and percentage of astrocytes within each cluster (**Supplemental Figure 2D**). Once these results were confirmed, we took each of these clusters and plotted the average z-scored calcium waveform peri-event within the –7.5 to 15 second window surrounding foot shock to understand if different functional subpopulations existed in response to fearful stimuli (**Supplemental Figure 2B**).

Statistical Methods

All statistical analyses were conducted using Python and GraphPad Prism v10. Details of the statistical tests, including the type of test used, sample sizes (n values), test statistics, p-values, post-hoc multiple comparisons, and any outlier removals, are provided in the text and figure legends where applicable.

Normality and Outlier Testing

To ensure the validity of our analyses, data normality was evaluated using the Shapiro-Wilk and Kolmogorov-Smirnov tests. Equality of variance was assessed using the Brown-Forsythe test. Outliers were identified using the ROUT method, as recommended by GraphPad Prism. This method relies on nonlinear regression to detect outliers, with a ROUT coefficient Q value set at 10% to increase the power of detection while maintaining a relatively lenient threshold. No outliers were detected across any analyses performed.

Peri-Event Analysis

For event-triggered average significance (foot shock), we used a tCI confidence interval method previously proposed [42]. For our event triggered averages we aggregated all within-animal signals so that we could assume that our samples were independent and identically distributed. Thus, for this method we assumed each time point was distributed according to a student-t's distribution. We then marked any period greater than 0.8 s (this decision was arbitrary and could be chosen to be longer for more conservative estimation, but this is longer than the proposed time threshold in the original paper) that did not include the baseline of 0 (traces were median-shifted to zero) was marked as a significant peri-event.

Hierarchical Bayesian Model

The hierarchical Bayesian model we implement here assumes each cell increases its activity from baseline level a_0 according to its Gaussian shaped temporal receptive field. To account for the variability across sequences, we assume that the peak location μ_i is estimated separately for the i^{th} sequence while the field width of σ and height of a_1 are fixed across sequences (**Figure 2D**). Therefore, at each time t after the onset of a foot shock (fear conditioning) or high internal activity (detected by event detector), the expected activity λ is:

$$\lambda(t) = a_1 \frac{1}{\sigma\sqrt{2\pi}} e^{-\frac{1}{2}\left(\frac{t-\mu_i}{\sigma}\right)^2} + a_0 + \epsilon$$

where the small Gaussian error term ϵ is centered at zero with a small fixed standard deviation calculated as three times the standard deviation of the entire session for each cell. In addition, we assume that μ_i is sampled from a normal distribution centered at M that captures the overall central tendency of the peak and standard deviation σ_t that estimate the between sequence variability to allow for a more accurate estimation of the temporal receptive field width [19].

The posterior distributions of estimated parameters were generated through the rStan package with four independent Markov-Chain-Monte-Carlo (MCMC) chains (3750 warm-up iterations and 250 post warm-up samples in each MCMC chain). The mode of the posterior distribution was then used to perform additional statistical analysis in the Result section.

References.

1. O'Keefe, J. & Dostrovsky, J. The hippocampus as a spatial map. Preliminary evidence from unit activity in the freely-moving rat. *Brain Res.* **34**, 171–175 (1971).

2. O'Keefe, J. Place units in the hippocampus of the freely moving rat. *Exp. Neurol.* **51**, 78–109 (1976).
3. O'Keefe, J. & Speakman, A. Single unit activity in the rat hippocampus during a spatial memory task. *Exp. Brain Res.* **68**, 1–27 (1987).
4. McNaughton, B. L., Battaglia, F. P., Jensen, O., Moser, E. I. & Moser, M.-B. Path integration and the neural basis of the "cognitive map." *Nat. Rev. Neurosci.* **7**, 663–678 (2006).
5. Eichenbaum, H. Time cells in the hippocampus: a new dimension for mapping memories. *Nat. Rev. Neurosci.* **15**, 732–744 (2014).
6. Mau, W. *et al.* The Same Hippocampal CA1 Population Simultaneously Codes Temporal Information over Multiple Timescales. *Curr. Biol.* **28**, 1499-1508.e4 (2018).
7. Curreli, S., Bonato, J., Romanzi, S., Panzeri, S. & Fellin, T. Complementary encoding of spatial information in hippocampal astrocytes. *PLoS Biol.* **20**, e3001530 (2022).
8. Doron, A. *et al.* Hippocampal astrocytes encode reward location. *Nature* **609**, 772–778 (2022).
9. Polykretis, I. & Michmizos, K. P. The role of astrocytes in place cell formation: A computational modeling study. *J. Comput. Neurosci.* **50**, 505–518 (2022).
10. Sheintuch, L. *et al.* Tracking the Same Neurons across Multiple Days in Ca2+ Imaging Data. *Cell Rep.* **21**, 1102–1115 (2017).
11. Suthard, R. L. *et al.* Basolateral Amygdala Astrocytes Are Engaged by the Acquisition and Expression of a Contextual Fear Memory. *J. Neurosci.* **43**, 4997–5013 (2023).
12. Suthard, R. L. *et al.* Engram reactivation mimics cellular signatures of fear. *Cell Rep.* **43**, 113850 (2024).
13. Qin, H. *et al.* Monitoring Astrocytic Ca2+ Activity in Freely Behaving Mice. *Front. Cell. Neurosci.* **14**, 603095 (2020).
14. Lee, E. K. *et al.* Non-linear dimensionality reduction on extracellular waveforms reveals cell type diversity in premotor cortex. *Elife* **10**, (2021).
15. Lee, K., Carr, N., Perliss, A. & Chandrasekaran, C. WaveMAP for identifying putative cell types from in vivo electrophysiology. *STAR Protoc* **4**, 102320 (2023).
16. MacDonald, C. J., Lepage, K. Q., Eden, U. T. & Eichenbaum, H. Hippocampal "time cells" bridge the gap in memory for discontiguous events. *Neuron* **71**, 737–749 (2011).

17. Cruzado, N. A., Tiganj, Z., Brincat, S. L., Miller, E. K. & Howard, M. W. Conjunctive representation of what and when in monkey hippocampus and lateral prefrontal cortex during an associative memory task. *Hippocampus* **30**, 1332–1346 (2020).
18. Taxidis, J. *et al.* Differential Emergence and Stability of Sensory and Temporal Representations in Context-Specific Hippocampal Sequences. *Neuron* **108**, 984-998.e9 (2020).
19. Cao, R., Bladon, J. H., Charczynski, S. J., Hasselmo, M. E. & Howard, M. W. Internally generated time in the rodent hippocampus is logarithmically compressed. *Elife* **11**, (2022).
20. Watanabe, S. Asymptotic equivalence of Bayes cross validation and widely applicable information criterion in singular learning theory. *J. Mach. Learn. Res.* **abs/1004.2316**, (2010).
21. Buzsáki, G. & Mizuseki, K. The log-dynamic brain: how skewed distributions affect network operations. *Nat. Rev. Neurosci.* **15**, 264–278 (2014).
22. Gomez, J. A. *et al.* Ventral tegmental area astrocytes orchestrate avoidance and approach behavior. *Nat. Commun.* **10**, 1455 (2019).
23. Mu, Y. *et al.* Glia accumulate evidence that actions are futile and suppress unsuccessful behavior. *Cell* **178**, 27-43.e19 (2019).
24. Cho, W.-H. *et al.* Hippocampal astrocytes modulate anxiety-like behavior. *Nat. Commun.* **13**, 6536 (2022).
25. Noh, K. *et al.* Cortical astrocytes modulate dominance behavior in male mice by regulating synaptic excitatory and inhibitory balance. *Nat. Neurosci.* **26**, 1541–1554 (2023).
26. Adamsky, A. *et al.* Astrocytic activation generates DE Novo neuronal potentiation and memory enhancement. *Cell* **174**, 59-71.e14 (2018).
27. Kol, A. *et al.* Astrocytes contribute to remote memory formation by modulating hippocampal-cortical communication during learning. *Nat. Neurosci.* **23**, 1229–1239 (2020).
28. Martin-Fernandez, M. *et al.* Synapse-specific astrocyte gating of amygdala-related behavior. *Nat. Neurosci.* **20**, 1540–1548 (2017).
29. Shikano, Y., Ikegaya, Y. & Sasaki, T. Minute-encoding neurons in hippocampal-striatal circuits. *Curr. Biol.* **31**, 1438-1449.e6 (2021).
30. Cahill, M. K. *et al.* Network-level encoding of local neurotransmitters in cortical astrocytes. *Nature* **629**, 146–153 (2024).

31. Lefton, K. B. *et al.* Norepinephrine Signals Through Astrocytes To Modulate Synapses. *bioRxiv* 2024.05.21.595135 (2024) doi:10.1101/2024.05.21.595135.
32. Haydon, P. G. GLIA: listening and talking to the synapse. *Nat. Rev. Neurosci.* **2**, 185–193 (2001).
33. Perea, G., Navarrete, M. & Araque, A. Tripartite synapses: astrocytes process and control synaptic information. *Trends Neurosci.* **32**, 421–431 (2009).
34. De Pittà, M., Brunel, N. & Volterra, A. Astrocytes: Orchestrating synaptic plasticity? *Neuroscience* **323**, 43–61 (2016).
35. Lacagnina, A. F. *et al.* Distinct hippocampal engrams control extinction and relapse of fear memory. *Nat. Neurosci.* **22**, 753–761 (2019).
36. Wang, C. *et al.* Microglia mediate forgetting via complement-dependent synaptic elimination. *Science* **367**, 688–694 (2020).
37. Chen, R. *et al.* Destabilization of fear memory by Rac1-driven engram-microglia communication in hippocampus. *Brain Behav. Immun.* **119**, 621–636 (2024).
38. Steadman, P. E. *et al.* Disruption of oligodendrogenesis impairs memory consolidation in adult mice. *Neuron* **105**, 150-164.e6 (2020).
39. Sun, W. *et al.* Spatial transcriptomics reveal neuron-astrocyte synergy in long-term memory. *Nature* **627**, 374–381 (2024).
40. Navarrete, M., Serra, I., Quintanilla, J. & García-Marqués, J. Catching astrocyte ensembles: Astrocytic ensembles control cue-motivated behavior. *Research Square* (2023) doi:10.21203/rs.3.rs-3427853/v1.
41. Zong, W. *et al.* Large-scale two-photon calcium imaging in freely moving mice. *Cell* **185**, 1240-1256.e30 (2022).
42. Jean-Richard-Dit-Bressel, P., Clifford, C. W. G. & McNally, G. P. Analyzing Event-Related Transients: Confidence Intervals, Permutation Tests, and Consecutive Thresholds. *Front. Mol. Neurosci.* **13**, 14 (2020).